Quantum Chromodynamics

Hsiang-nan Li
Institute of Physics, Academia Sinica, Taipei, Taiwan 115, Republic of China

Abstract

I review the basics of perturbative QCD, including infrared divergences and safety, collinear and k_T factorization theorems, and various evolution equations and resummation techniques for single- and double-logarithmic corrections. I then elaborate its applications to studies of jet substructures and hadronic two-body heavy-quark decays.

1 Introduction

One of the important missions of the Large Hadron Collider (LHC) is to search for new physics beyond the standard model. The identification of new physics signals usually requires precise understanding of standard-model background, whose contributions mainly arise from quantum chromodynamics (QCD). Many theoretical approaches have been developed based on QCD, which are appropriate for studies of processes in different kinematic regions and involving different hadronic systems. The theoretical framework for high-energy hadron collisions is known as the perturbative QCD (pQCD). I will focus on pQCD below, introducing its fundamental ingredients and applications to LHC physics. Supplementary material can be found in [1].

The simple QCD Lagrangian reveals rich dynamics. It exhibits the confinement at low energy, which accounts for the existence of various hadronic bound states, such as pions, protons, B mesons, and etc.. This nonperturbative dynamics is manifested by infrared divergences in perturbative calculations of bound-state properties like parton distribution functions and fragmentation functions. On the other hand, the asymptotic freedom at high energy leads to a small coupling constant, that allows formulation of pQCD. Therefore, it is possible to test QCD in high-energy scattering, which is, however, nontrivial due to bound-state properties of involved hadrons. That is, high-energy QCD processes still involve both perturbative and nonperturbative dynamics. A sophisticated theoretical framework needs to be established in order to realize the goal of pQCD: it is the factorization theorem [2], in which infrared divergences are factorized out of a process, and the remaining piece goes to a hard kernel. The point is to prove the universality of the infrared divergences, namely, the independence of processes the same hadron participates in. Then the infrared divergences are absorbed into a parton distribution function (PDF) for the hadron, which just needs to be determined once, either from experimental data or by nonperturbative methods. The universality of a PDF guarantees the infrared finiteness of hard kernels for all processes involving the same hadron. Convoluting these hard kernels with the determined PDF, one can make predictions. In other words, the universality of a PDF warrants the predictive power of the factorization theorem.

Though infrared divergences are factorized into a PDF, the associated logarithmic terms may appear in a process, that is not fully inclusive. To improve perturbative expansion, these logarithmic corrections should be organized by evolution equations or resummation techniques. For the summation of different single logarithms, the Dokshitzer-Gribov-Lipatov-Altarelli-Parisi (DGLAP) equation [3] and the Balitsky-Fadin-Kuraev-Lipatov (BFKL) equation [4] have been proposed. For different double logarithms, the threshold resummation [5–7] and the k_T resummation [8,9] have been developed. Besides, an attempt has been made to combine the DGLAP and BFKL equations, leading to the Ciafaloni-Catani-Fiorani-Marchesini (CCFM) equation [10]. Similarly, the threshold and k_T resummations has been unified under the joint resummation [11,12], which is applicable to processes in a wider kinematic range. A simple framework for understanding all the above evolution equations and resummation techniques will be provided.

After being equipped with the pQCD formalism, we are ready to learn its applications to various processes, for which I will introduce jet substructures and hadronic two-body heavy-quark decays. It will be demonstrated that jet substructures, information which is crucial for particle identification at the LHC and usually acquired from event generators [13], are actually calculable using the resummation technique. Among jet substructures investigated in the literature, the distribution in jet invariant mass and the energy profile within a jet cone will be elaborated. For the latter, it will be shown that the factorization theorem goes beyond the conventional naive factorization assumption [14], and provides valuable predictions for branching ratios and CP asymmetries of hadronic two-body heavy-quark decays, that can be confronted by LHCb data. Specifically, I will concentrate on three major approaches, the QCD-improved factorization [15], the perturbative QCD [16–19], and the soft-collinear-effective theory [20–23]. Some long-standing puzzles in B meson decays and their plausible resolutions are reviewed. For more details on this subject, refer to [24].

2 Factorization Theorem

The QCD lagrangian is written as

$$\mathcal{L}_{QCD} = \bar{\psi}(i \not{D}_a T_a - m)\psi - \frac{1}{4}F_a^{\mu\nu}F_{\mu\nu a}, \tag{1}$$

with the quark field ψ, the quark mass m, and the covariant derivative and the gauge field tensor

$$
\begin{aligned}
D_a^\mu &= \partial^\mu + igA_a^\mu, \\
F_a^{\mu\nu} &= \partial^\mu A_a^\nu - \partial^\nu A_a^\mu - gf_{abc}A_b^\mu A_c^\nu,
\end{aligned} \tag{2}
$$

respectively. The color matrices T_a and the structure constants f_{abc} obey

$$[T_a^{(F)}, T_b^{(F)}] = if_{abc}T_c^{(F)}, \quad (T_a^{(A)})_{bc} = -if_{abc}, \tag{3}$$

where F (A) denotes the fundamental (adjoint) representation. Adding the gauge-fixing term in the path-integral quantization to remove spurious degrees of freedom, Eq. (1) becomes

$$\mathcal{L}_{QCD} = \bar{\psi}(i \not{D}_a T_a - m)\psi - \frac{1}{4}F_a^{\mu\nu}F_{\mu\nu a} - \frac{1}{2}\lambda(\partial_\mu A_a^\mu)^2 + \partial_\mu \eta_a^\dagger(\partial^\mu + gf_{abc}A_c^\mu)\eta_b, \tag{4}$$

with the gauge parameter λ, and the ghost field η. The last term in the above expression comes from the Jacobian for the variable change, as fixing the gauge.

The Feynman rules for QCD can be derived from Eq. (4) following the standard procedures [25]. The quark and gluon propagators with the momentum p are given by $i\not{p}/(p^2 + i\epsilon)$ and $-ig^{\mu\nu}/p^2$ in the Feynman gauge, respectively. The quark-gluon-quark vertex and the ghost-gluon-ghost vertex are written as $-ig\gamma_\mu T_a$ and $gf_{abc}p'_\mu$, respectively, where the subscripts μ and a are associated with the gluon, p' is the momentum of the outgoing ghost, and b (c) is associated with the outgoing (incoming) ghost. The three-gluon vertex and the four-gluon vertex are given by

$$
\begin{aligned}
\Gamma_{3g} &= -gf_{a_1a_2a_3}[g^{\nu_1\nu_2}(p_1 - p_2)^{\nu_3} + g^{\nu_2\nu_3}(p_2 - p_3)^{\nu_1} + g^{\nu_3\nu_1}(p_3 - p_1)^{\nu_2}, \\
\Gamma_{4g} &= -ig^2[f_{ea_1a_2}f_{ea_3a_4}(g^{\nu_1\nu_3}g^{\nu_2\nu_4} - g^{\nu_1\nu_4}g^{\nu_2\nu_3}) + f_{ea_1a_3}f_{ea_4a_2}(g^{\nu_1\nu_4}g^{\nu_3\nu_2} - g^{\nu_1\nu_2}g^{\nu_3\nu_4}) \\
&\quad + f_{ea_1a_4}f_{ea_2a_3}(g^{\nu_1\nu_2}g^{\nu_4\nu_3} - g^{\nu_1\nu_3}g^{\nu_4\nu_2})],
\end{aligned} \tag{5}
$$

respectively, where the subscripts a_1, a_2, $\cdots$ and ν_1, ν_2, $\cdots$ are assigned to gluons counterclockwise. The particle momenta flow into the vertices in all the above Feynman rules.

2.1 Infrared Divergences and Safety

The first step to establish the factorization theorem is to identify infrared divergences in Feynman diagrams for a QCD process at quark-gluon level. We start with the vertex correction to the amplitude $\gamma^*(q) \to q(p_1)\bar{q}(p_2)$, in which a virtual photon of momentum $q = p_1 + p_1$ splits into a quark of momentum p_1 and an anti-quark of momentum p_2. Given the Feynman rules, one has the loop integral

$$\int \frac{d^4 l}{(2\pi)^4}(-ig\gamma^\nu T_a)\frac{i(\not{p}_1 - \not{l})}{(p_1-l)^2+i\epsilon}(-ie\gamma_\mu)\frac{-i(\not{p}_2-\not{l})}{(p_2-l)^2+i\epsilon}(-ig\gamma_\nu T_a)\frac{-i}{l^2+i\epsilon}, \tag{6}$$

where l is the loop momentum carried by the gluon, and the inclusion of the corresponding counterterm for the regularization of a ultraviolet divergence is understood. The appearance of infrared divergences becomes more transparent, as performing the contour integration in the light-cone frame, in which the coordinates $l^\mu = (l^+, l^-, \mathbf{l}_T)$ are defined by

$$l^\pm = \frac{l^0 \pm l^z}{\sqrt{2}}, \quad \mathbf{l}_T = (l^x, l^y). \tag{7}$$

When an on-shell particle moves along the light cone, only one component of its momentum is large in this frame. For example, the above quark momenta can be chosen as $p_1^\mu = (p_1^+, 0, \mathbf{0}_T)$ and $p_2^\mu = (0, p_2^-, \mathbf{0}_T)$.

In terms of the light-cone coordinates, Eq. (6) is reexpressed as

$$\int \frac{dl^+ dl^- d^2 l_T}{(2\pi)^4} \frac{1}{2(l^+ - p_1^+)l^- - l_T^2 + i\epsilon} \frac{1}{2l^+(l^- - p_2^-) - l_T^2 + i\epsilon} \frac{1}{2l^+ l^- - l_T^2 + i\epsilon}, \tag{8}$$

where only the denominators are shown, since infrared divergences are mainly determined by pole structures. The poles of l^- are located, for $0 < l^+ < p_1^+$, at

$$l^- = \frac{l_T^2}{2(l^+ - p_1^+)} + i\epsilon, \quad l^- = p_2^- + \frac{l_T^2}{2l^+} - i\epsilon, \quad l^- = \frac{l_T^2}{2l^+} - i\epsilon. \tag{9}$$

As $l^+ \sim O(p_1^+)$, the contour of l^- is pinched at $l^- \sim O(l_T^2/p_1^+)$ by the first and third poles, defining the collinear region. As $l^+ \sim O(l_T)$, the contour of l^- is pinched at $l^- \sim O(l_T)$, defining the soft region. That is, the collinear (soft) region corresponds to the configuration of $l^\mu \sim (E, \Lambda^2/E, \Lambda)$ $(l^\mu \sim (\Lambda, \Lambda, \Lambda))$, where E and Λ denote a large scale and a small scale, respectively. Another leading configuration arises from the hard region characterized by $l^\mu \sim (E, E, E)$. A simple power counting implies that all the above three regions give logarithmic divergences. Picking up the first pole in Eq. (9), Eq. (8) becomes

$$\frac{-i}{2p_1^+}\int \frac{dl^+ d^2 l_T}{(2\pi)^3}\frac{p_1^+ - l^+}{2p_2^- l^+(p_1^+ - l^+) + p_1^+ l_T^2}\frac{1}{l_T^2} \approx \frac{-i}{4p_1 \cdot p_2}\frac{1}{(2\pi)^3}\int \frac{dl^+}{l^+}\int \frac{d^2 l_T}{l_T^2}, \tag{10}$$

which produces the double logarithm from the overlap of the collinear (the integration over l^+) and soft (the integration over l_T) enhancements.

The existence of infrared divergences is a general feature of QCD corrections. An amplitude is not a physical quantity, but a cross section is. To examine whether the infrared divergences really call for attention, we extend the calculation to the cross section of the process $e^- e^+ \to X$, the $e^- e^+$ annihilation into hadrons. A cross section is computed as the square of an amplitude, whose Feynman diagrams are composed of those for the amplitude connected by their complex conjugate with a final-state cut between them. The cross section at the Born level $e^- e^+ \to \gamma^* \to q\bar{q}$ is written as

$$\sigma^{(0)} = N_c \frac{4\pi\alpha^2}{3Q^2}\sum_f Q_f^2, \tag{11}$$
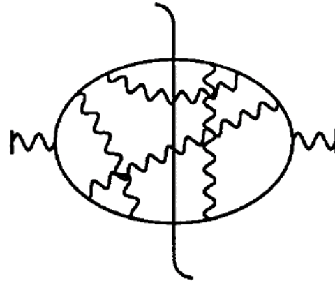
Fig. 1: Final-state cut on self-energy corrections to a virtual photon propagator.

where $N_c = 3$ is the number of colors, α is the electromagnetic coupling constant, Q^2 is the $e^- e^+$ invariant mass, and Q_f is the quark charge in units of the electron charge. The virtual one-loop corrections, including those to the gluon vertex in Eq. (6) and to the quark self-energy, give in the dimensional regularization [25]

$$\sigma^{(1)V} = -2N_c C_F \sum_f Q_f^2 \frac{\alpha \alpha_s}{\pi} Q^2 \left(\frac{4\pi\mu^2}{Q^2}\right)^{2\epsilon} \frac{1-\epsilon}{\Gamma(2-2\epsilon)} \left[\frac{1}{\epsilon^2} + \frac{3}{2}\frac{1}{\epsilon} - \frac{\pi^2}{2} + 4 + O(\epsilon)\right], \qquad (12)$$

with the color factor $C_F = 4/3$, the strong coupling constant α_s, the renormalization scale μ, and the Gamma function Γ. The double pole $1/\epsilon^2$ is a consequence of the overlap of the collinear and soft divergences. The one-loop corrections from real gluons lead to [25]

$$\sigma^{(1)R} = 2N_c C_F \sum_f Q_f^2 \frac{\alpha \alpha_s}{\pi} Q^2 \left(\frac{4\pi\mu^2}{Q^2}\right)^{2\epsilon} \frac{1-\epsilon}{\Gamma(2-2\epsilon)} \left[\frac{1}{\epsilon^2} + \frac{3}{2}\frac{1}{\epsilon} - \frac{\pi^2}{2} + \frac{19}{4} + O(\epsilon)\right]. \qquad (13)$$

It is a crucial observation that the infrared divergences cancel in the summation over the virtual and real corrections in Eqs. (12) and (13), respectively: the double and single poles have a minus sign in the former, but a plus sign in the latter. It is easy to understand the infrared cancellation by means of self-energy corrections to the propagator of a virtual photon. Since a virtual photon does not involve a low characteristic scale, the loop corrections must be infrared finite. As taking the final-state cut shown in Fig. 1, the imaginary piece of a particle propagator is picked up, $\text{Im}(1/(p^2 + i\epsilon)) \propto \delta(p^2)$, which corresponds to the Feynman rule for an on-shell particle. Because the self-energy corrections are infrared finite, their imaginary part, i.e., the $e^- e^+ \to X$ cross section, is certainly infrared finite. The above observation has been formulated into the Kinoshita-Lee-Nauenberg (KLN) theorem [26], which states that a cross section is infrared safe, as integrating over all phase spaces of final states. Combining Eqs. (11), (12), and (13), one derives the $e^- e^+ \to X$ cross section up to next-to-leading order (NLO)

$$\sigma = N_c \frac{4\pi\alpha^2}{3Q^2} \sum_f Q_f^2 \left[1 + \frac{3}{4}\frac{\alpha_s(Q)}{\pi} C_F\right], \qquad (14)$$

that has been used to determine the strong coupling constant $\alpha_s(Q)$ at the scale Q.

2.2 DIS and Collinear Factorization

Though a naive perturbation theory applies to the $e^- e^+$ annihilation, it fails for more complicated ones, such as the deeply inelastic scattering (DIS) of a nucleon by a lepton, $\ell(k)N(p) \to \ell(k') + X$. Even as the momentum transfer squared $-q^2 = (k - k')^2 \equiv Q^2$ is large, the quark-level cross section for the DIS suffers infrared divergences at high orders, which reflect the nonperturbative dynamics in the nucleon. A special treatment of the infrared divergences is then required. It will be demonstrated that they can be factorized out of the scattering process, and absorbed into a nucleon PDF.

QUANTUM CHROMODYNAMICS

Consider the two structure functions $F_{1,2}(x, Q^2)$ involved in the DIS, where the Bjorken variable is defined as $x \equiv -q^2/(2p \cdot q) = Q^2/(2p \cdot q)$, and take F_2 as an example. We shall not repeat loop integrations, but quote the NLO corrections to the quark-level diagrams [25]:

$$
\begin{aligned}
F_2^q(x, Q^2) &= x \left\{ \delta(1-x) + \frac{\alpha_s}{2\pi} C_F \left[\frac{1+x^2}{1-x} \left(\ln\frac{1-x}{x} - \frac{3}{4} \right) + \frac{1}{4}(9+5x) \right]_+ \right. \\
&\quad \left. + \frac{\alpha_s}{2\pi} C_F \left(\frac{1+x^2}{1-x} \right)_+ \left(4\pi\mu e^{-\gamma_E} \right)^\epsilon \int_0^{Q^2} \frac{dk_T^2}{k_T^{2+2\epsilon}} + \cdots \right\},
\end{aligned}
$$

(15)

where the superscript q denotes the initial-state quark, γ_E is the Euler constant, and the first term comes from the leading-order (LO) contribution. The subscript $+$ represents the plus function, which is understood as a distribution function via

$$
\int_0^1 dx \frac{f(x)}{(1-x)_+} \equiv \int_0^1 dx \frac{f(x) - f(1)}{1-x}.
$$

(16)

The integration over k_T^2 generates an infrared divergence, that is regularized in the dimensional regularization with $\epsilon < 0$,

$$
\int_0^{Q^2} \frac{dk_T^2}{k_T^{2+2\epsilon}} = \frac{1}{-\epsilon} \left(Q^2 \right)^{-\epsilon}.
$$

(17)

Hence, the infrared divergence does exist in the perturbative evaluation of the DIS structure function, even after summing over the virtual and real corrections. This divergence arises from the collinear region with the loop momentum being parallel to the nucleon momentum, since it can also be regularized by introducing a mass to the initial-state quark. It is related to the confinement mechanism, and corresponds to a long-distance phenomenon associated with a group of collimated on-shell particles. The other terms in Eq. (15) represent the hard NLO contribution to the structure function. Comparing the results for the DIS and for the e^-e^+ annihilation, the former involves the integration over final-state kinematics, but not over initial-state kinematics. This is the reason why the KLN theorem does not apply to the infrared divergences associated with the initial-state nucleon, and the above collinear divergence exists. Note that the soft divergences cancel between virtual and real diagrams due to the fact that a nucleon is color-singlet: a soft gluon with a huge space-time distribution cannot resolve the color structure of a nucleon, so it does not interact with it.

Besides, the collinear gluon emissions modify a quark momentum, such that the initial-state quark can carry various momenta, as it participates in hard scattering. It is then natural to absorb the collinear divergences into a PDF for the nucleon, $\phi_{q/N}$, which describes the probability for quark q to carry certain amount of the nucleon momentum. In other words, the quark-level collinear divergences are subtracted by those in the PDF in perturbation theory, and the remaining infrared finite piece contributes to the hard kernel H. We write the quark-level structure function as the following expansion in the strong coupling constant,

$$
F_2^q(x, Q^2) = H^{(0)} \otimes \phi_{f/N}^{(0)} + \frac{\alpha_s}{2\pi} H^{(1)} \otimes \phi_{q/N}^{(0)} + \frac{\alpha_s}{2\pi} H^{(0)} \otimes \phi_{q/N}^{(1)} + \cdots,
$$

(18)

where $H^{(i)}$ ($\phi_{q/N}^{(i)}$) is the hard kernel (PDF) of the i-th order. The symbol $\otimes$ represents a convolution in the parton momentum fraction ξ:

$$
H \otimes \phi_{q/N} \equiv \int_x^1 \frac{d\xi}{\xi} H(x/\xi, Q, \mu) \phi_{q/N}(\xi, \mu).
$$

(19)

99

We are ready to assign each term in Eq. (15) into either $H^{(i)}$ or $\phi_{q/N}^{(i)}$. The first term $\delta(1-x)$ goes to $H^{(0)} \otimes \phi_{q/N}^{(0)}$ with the definitions

$$H^{(0)}(x/\xi, Q, \mu) = \delta(1 - x/\xi), \quad \phi_{q/N}^{(0)}(\xi,\mu) = \delta(1 - \xi), \tag{20}$$

which confirm $H^{(0)} \otimes \phi_{q/N}^{(0)} = \delta(1 - x)$. The second term in Eq. (15) is assigned to $H^{(1)} \otimes \phi_{q/N}^{(0)}$ and the third term to $H^{(0)} \otimes \phi_{q/N}^{(1)}$ with

$$H^{(1)}(x, Q, \mu) = P_{qq}^{(1)}(x) \ln \frac{Q^2}{\mu^2} + \cdots,$$
$$\phi_{q/N}^{(1)}(\xi,\mu) = \left(4\pi\mu e^{-\gamma}\right)^\epsilon P_{qq}^{(1)}(\xi) \int_0^{\mu^2} \frac{dk_T^2}{k_T^{2+2\epsilon}}, \tag{21}$$

and the quark splitting function

$$P_{qq}^{(1)}(x) = C_F \left(\frac{1 + x^2}{1 - x}\right)_+. \tag{22}$$

The definition of the PDF in terms of a hadronic matrix element is given by

$$\phi_{q/N}(\xi,\mu) = \int \frac{dy^-}{2\pi} \exp(-i\xi p^+ y^-)$$
$$\times \frac{1}{2} \sum_\sigma \langle N(p,\sigma)|\bar{q}(0, y^-, 0_T)\frac{1}{2}\gamma^+ W(y^-, 0)q(0, 0, 0_T)|N(p,\sigma)\rangle, \tag{23}$$

where $|N(p,\sigma)\rangle$ denotes the bound state of the nucleon with momentum p and spin σ, y^- is the minus component of the coordinate of the quark field after the final-state cut, the first factor $1/2$ is attributed to the average over the nucleon spin, and the matrix $\gamma^+/2$ is the spin projector for the nucleon. Here μ is called the factorization scale, which is similar to a renormalization scale, but introduced in perturbative computations for an effective theory. The Wilson lines are defined by $W(y^-, 0) = W(0)W^\dagger(y^-)$ with

$$W(y^-) = \mathcal{P}\exp\left[-ig \int_0^\infty dz n_- \cdot A(y + zn_-)\right], \tag{24}$$

where $\mathcal{P}$ represents a path-ordered exponential. The Wilson line behaves like a scalar particle carrying a color source. The two quark fields in Eq. (23) are separated by a distance, so the above Wilson links are demanded by the gauge invariance of the nonlocal matrix element. Since Eq. (23) depends only on the property of the nucleon, but not on the hard processes it participates in, a PDF is universal (process-independent). This is the most important observation, that warrants the predictive power of the factorization theorem.

The Wilson line appears as a consequence of the eikonalization of the final-state quark, to which the collinear gluons attach. The eikonalization is illustrated below by considering the loop correction to the virtual photon vertex. Assuming the initial-state quark momentum $p = (p^+, 0, \mathbf{0_T})$ and the final-state quark momentum $p' = (0, p'^-, \mathbf{0_T})$, we have the partial integrand

$$\not{p}'\gamma^\nu \frac{\not{p}' + \not{l}}{(p' + l)^2}\gamma^\mu \frac{\not{p} + \not{l}}{(p + l)^2}\gamma_\nu \approx \not{p}'\gamma^- \frac{\not{p}' + \not{l}}{(p' + l)^2}\gamma^\mu \frac{\not{p} + \not{l}}{(p + l)^2}\gamma^+ \approx \not{p}'\gamma^- \frac{\not{p}'}{2p' \cdot l}\gamma^\mu \frac{\not{p} + \not{l}}{(p + l)^2}\gamma^+, \tag{25}$$

as the loop momentum l is collinear to p, where $\not{p}'$ comes from the Feynman rule for the final-state quark, γ^μ is the photon vertex, and the subleading contribution from the transverse components of γ^ν has been

neglected. Applying the identity $\gamma^- \not{p}' = 2p'^- - \not{p}'\gamma^-$ and $\not{p}' \not{p}' = p'^2 = 0$ leads the above expression to

$$\not{p}'\gamma^\mu \frac{\not{p}+\not{l}}{(p+l)^2}\gamma^+ \frac{p'^-}{p'\cdot l} \approx \not{p}'\gamma^\mu \frac{\not{p}+\not{l}}{(p+l)^2}\gamma^+ \frac{n_-^-}{n_-\cdot l} \approx \not{p}'\gamma^\mu \frac{\not{p}+\not{l}}{(p+l)^2}\gamma_\nu \frac{n_-^\nu}{n_-\cdot l}, \tag{26}$$

where the dimensionless vector $n_- = (0, 1, \mathbf{0_T})$ is parallel to p', and the subleading contribution from $\nu = T$ has been restored. The factor n_-^ν and $1/n_- \cdot l$ are called the eikonal vertex and the eikonal propagator, respectively.

It is then shown that the Feynman rule $n_-^\nu / n_- \cdot l$ for the eikonalized final-state quark is derived from the Wilson line in Eq. (24). Consider the expansion of the path-order exponential in $W(0)$ up to order of α_s, and Fourier transform the gauge field into the momentum space,

$$-ig \int_0^\infty dz n_- \cdot \int d^4 l \exp[iz(n_-\cdot l + i\epsilon)]\tilde{A}(l)$$

$$= -ig \int d^4 l \frac{\exp[iz(n_-\cdot l + i\epsilon)]}{i(n_-\cdot l + i\epsilon)}\bigg|_{z=0}^{z=\infty} n_- \cdot \tilde{A}(l) = \int d^4 l \frac{gn_-^\nu}{n_-\cdot l + i\epsilon}\tilde{A}_\nu(l), \tag{27}$$

where the term $i\epsilon$ has been introduced to suppress the contribution from $z = \infty$. The field $\tilde{A}(l)$ is contracted with the gauge field from the initial-state quark with interaction to form the gluon propagator $-i/(l^2 + i\epsilon)$. The expansion of the second piece $W(y^-)$ gives the Feynman rules for the eikonal propagator appearing after the final-state cut. In this case the additional exponential factor $\exp(il \cdot y)$ is combined with $\exp(-i\xi p^+ y^-)$, implying that the valence quark $q(0, y^-, 0_T)$ after the final-state cut carries the momentum $\xi p - l$. In summary, the first (second) piece of Wilson lines corresponds to the configuration without (with) the loop momentum flowing through the hard kernel. The above discussion verifies the Wilson lines in the PDF definition.

After detaching the collinear gluons from the final-state quark, the fermion flow still connects the PDF and the hard kernel. To achieve the factorization in the fermion flow, we insert the Fierz identity,

$$I_{ij}I_{lk} = \frac{1}{4}I_{ik}I_{lj} + \frac{1}{4}(\gamma_\alpha)_{ik}(\gamma^\alpha)_{lj} + \frac{1}{4}(\gamma^5\gamma_\alpha)_{ik}(\gamma^\alpha\gamma^5)_{lj}$$

$$+ \frac{1}{4}(\gamma^5)_{ik}(\gamma^5)_{lj} + \frac{1}{8}(\gamma^5\sigma_{\alpha\beta})_{ik}(\sigma^{\alpha\beta}\gamma^5)_{lj}, \tag{28}$$

with I being the identity matrix and $\sigma_{\alpha\beta} \equiv i[\gamma_\alpha, \gamma_\beta]/2$. At leading power, only the term $(\gamma_\alpha)_{ik}(\gamma^\alpha)_{lj}/4$ contributes, in which the structure $(\gamma^\alpha)_{lj}/2 \approx (\gamma^+)_{lj}/2$ goes to the definition of the PDF in Eq. (23), and $(\gamma_\alpha)_{ik}/2 \approx (\gamma^-)_{ik}/2$ goes into the evaluation of the hard kernel. The other terms in Eq. (28) contribute at higher powers. Similarly, we have to factorize the color flow between the PDF and the hard kernel by inserting the identity

$$I_{ij}I_{lk} = \frac{1}{N_c}I_{ik}I_{lj} + 2(T^c)_{ik}(T^c)_{lj}, \tag{29}$$

where I denotes the 3×3 identity matrix, and T^c is a color matrix. The first term in the above expression contributes to the present configuration, in which the valence quarks before and after the final-state cut are in the color-singlet state. The structure I_{lj}/N_c goes into the definition of the PDF, and I_{ik} goes into the evaluation of the hard kernel. The second term in Eq. (29) contributes to the color-octet state of the valence quarks, together with which an additional gluonic parton comes out of the nucleon and participates in the hard scattering.

The factorization formula for the nucleon DIS structure function is written as

$$F_2(x, Q^2) = \sum_f \int_x^1 \frac{d\xi}{\xi} H_f(x/\xi, Q, \mu)\phi_{f/N}(\xi, \mu), \tag{30}$$

with the subscript f labeling the parton flavor, such as a valence quark, a gluon, or a sea quark. The hard kernel H_f is obtained following the subtraction procedure for the collinear divergences, and its LO and NLO expressions have been presented in Eqs. (20) and (21), respectively. The universal PDF $\phi_{f/N}$, describing the probability for parton f to carry the momentum fraction ξ in the nucleon, takes a smooth model function. It must be derived by nonperturbative methods, or extracted from data.

2.3 Predictive Power

The factorization theorem derived above is consistent with the well-known parton model. The nucleon travels a long space-time, before it is hit by the virtual photon. As $Q^2 \gg 1$, the hard scattering occurs at point space-time. Relatively speaking, the quark in the nucleon behaves like a free particle before the hard scattering, and decouples from the rest of the nucleon. Therefore, the cross section for the nucleon DIS reduces to an incoherent sum over parton flavors under the collinear factorization. That is, the approximation

$$\left| \sum_i \mathcal{M}_{i/N} \right|^2 \approx \sum_i |\mathcal{M}_f|^2 \phi_{f/N}, \tag{31}$$

holds, where $\mathcal{M}_{i/N}$ represents the scattering amplitude for partonic state i of the nucleon N (it could be a multi-parton state), and $\mathcal{M}_f$ represents the infrared finite scattering amplitude for parton f.

Comparing the factorization theorem with the operator product expansion (OPE), the latter involves an expansion in short distance $y^\mu \sim 0$. A typical example is the infrared safe $e^- e^+ \to X$, whose cross section can be expressed as a series $\sigma \approx \sum_i C_i(y) O_i(0)$. The Wilson coefficients C_i and the local effective operators O_i appear in a product in the OPE. A factorization formula involves an expansion on the light cone with small $y^2 \sim 0$, instead of $y^\mu \sim 0$. A typical example is the DIS structure function, in which the existence of the collinear divergences implies that a parton travels a finite longitudinal distance y^-. It is also the reason why the hard kernel H_f and the PDF $\phi_{f/N}$ appear in a convolution in the momentum fraction.

The factorization procedure introduces the factorization scale μ into the hard kernel H_f and the PDF $\phi_{f/N}$, as indicated in Eq. (30). Higher-order corrections produce the logarithms $\ln(Q/\mu)$ in H_f and $\ln(\mu/Q_0)$ in $\phi_{f/N}$, which come from the splitting of $\ln(Q/Q_0)$ in the structure function F_2, Q_0 being a low scale characterizing $\phi_{f/N}$. One usually sets $\mu = Q$ to eliminate the logarithm in H_f, such that the input $\phi_{f/N}(\xi, Q)$ for arbitrary Q is needed. The factorization scale does not exist in QCD diagrams, but is introduced when a physical quantity like the structure function is factorized. The independence of the factorization scale, $\mu d F_2/d\mu = 0$, leads to a set of renormalization-group (RG) equations

$$\mu \frac{d}{d\mu} \phi_{f/N}(\xi, \mu) = \gamma_f \phi_{f/N}(\xi, \mu),$$
$$\mu \frac{d}{d\mu} H_f(x/\xi, Q, \mu) = -\gamma_f H_f(x/\xi, Q, \mu), \tag{32}$$

where γ_f denotes the anomalous dimension of the PDF. A solution of the RG equations describes the evolution of the PDF in Q

$$\phi_{f/N}(\xi, Q) = \phi_{f/N}(\xi, Q_0) \exp\left[\int_{Q_0}^{Q} \frac{d\mu}{\mu} \gamma_f(\alpha_s(\mu)) \right], \tag{33}$$

as a result of the all-order summation of $\ln(Q/Q_0)$. Hence, one just extracts the initial condition $\phi(\xi, Q_0)$ defined at the initial scale Q_0 from data. The PDF at other higher scales Q is known through the evolution. That is, the inclusion of the RG evolution increases the predictive power of the factorization theorem.
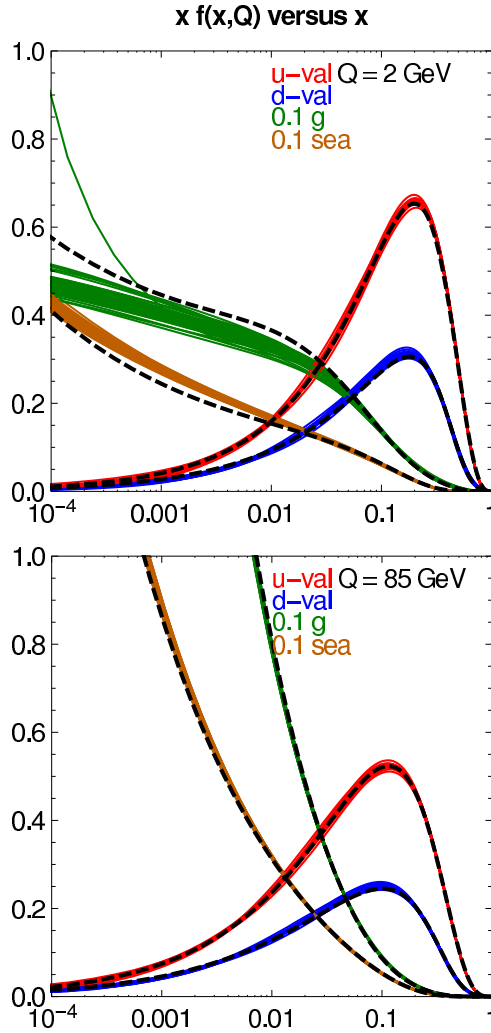
x f(x,Q) versus x

Fig. 2: CT10 NNLO (solid color) and NLO (dashed) parton distribution functions.

Fitting the factorization formulas for those processes, whose dynamics is believed to be clear, such as Eq. (30) for DIS, one has determined the PDFs for various partons in the proton. The CTEQ-TEA CT10 models at the accuracy of NLO and next-to-next-to-leading order (NNLO) for hard kernels are displayed in Figs. 2 [27, 28]. The increase of the gluon and sea-quark PDFs with the decrease of the momentum fraction ξ is a consequence of more radiations in that region in order to reach a lower ξ. The comparison of the PDFs at $Q = 2$ GeV and $Q = 85$ GeV indicates that the valence u-quark and d-quark PDFs become broader with Q, while the gluon and sea-quark PDFs increase with Q.

Note that a choice of an infrared regulator is, like an ultraviolet regulator, arbitrary; namely, we can associate an arbitrary finite piece with the infrared pole $1/(-\epsilon)$ in $\phi_{f/N}^{(1)}$. Shifts of different finite pieces between $\phi_{f/N}$ and H_f correspond to different factorization schemes. Hence, the extraction of a PDF depends not only on powers and orders, at which QCD diagrams are computed, but on factorization schemes. Since perturbative calculations are performed up to finite powers and orders, a factorization scheme dependence is unavoidable. Nevertheless, the scheme dependence of pQCD predictions would be minimized, if one sticks to the same factorization scheme. Before adopting models for PDFs, it should be checked at which power and order, at which initial scale, and in what scheme they are determined.

At last, I explain how to apply the factorization theorem to make predictions for QCD processes. A nucleon PDF $\phi_{f/N}$ is infrared divergent, if evaluated in perturbation theory due to the confinement mechanism. The QCD diagram for a DIS structure function involving quarks and gluons as the external
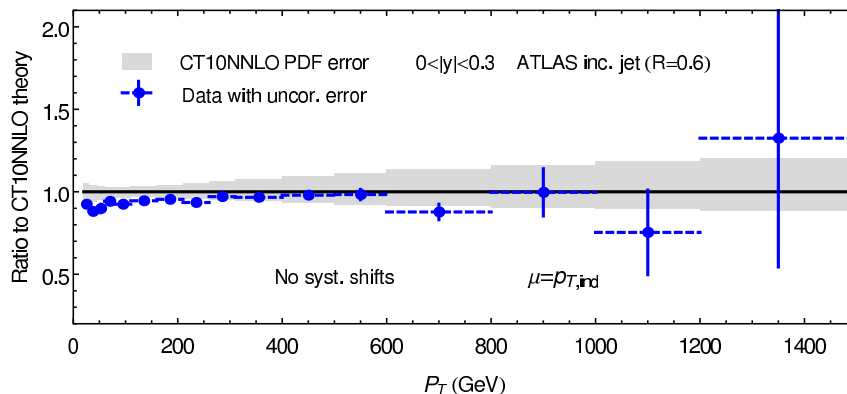
Fig. 3: Comparison of ATLAS data for inclusive jet p_T distribution with a theoretical prediction using CT10 NNLO.

particles are also infrared divergent. It has been demonstrated that the infrared divergences cancel between the QCD diagrams and the effective diagrams for $\phi_{f/N}$, as taking their difference, which defines the hard kernel H^{DIS}. One then derives the factorization formula for other processes, such as the Drell-Yan (DY) process $N(p_1)N(p_2) \to \ell^+\ell^-(q) + X$, and computes the corresponding hard kernel H^{DY}. The point is to verify that the infrared divergences in the QCD diagrams for DY and in the effective diagrams for the nucleon PDF cancel, and H^{DY} is infrared finite. If it is the case, the universality of the nucleon PDF holds, and the factorization theorem is applicable. If not, the factorization theorem fails. After verifying the factorization theorem, one makes predictions for the DY cross section using the formula $\sigma^{\mathrm{DY}} = \phi_{f_1/N} \otimes H^{\mathrm{DY}} \otimes \phi_{f_2/N}$. As an example, the predictions for the inclusive jet p_T distribution derived from the factorization theorem [28] are presented in Fig. 3. The consistency between the predictions and the ATLAS data is obvious.

2.4 k_T Factorization

The collinear factorization theorem introduced above has been intensively investigated and widely applied to many QCD processes up to higher powers and orders. The evolution of PDFs from low to high factorization scales is governed by the DGLAP equation. The databases for PDFs have been constructed, such as the CTEQ models. Other nonperturbative inputs like soft functions, jet functions, and fragmentation functions have been all explored to some extent. However, another more complicated framework, the k_T factorization theorem [29–31], may be more appropriate in some kinematic regions or in semi-inclusive processes. The collinear factorization applies, when the DIS is measured at a finite Bjorken variable x. The cross section is written as the convolution of a hard kernel with a PDF in a parton momentum fraction ξ. As $x \to 0$, $\xi \geq x$ can reach a small value, at which the parton transverse momentum k_T is of the same order of magnitude as the longitudinal momentum ξp, and not negligible. Once k_T is kept in a hard kernel, a transverse-momentum-dependent (TMD) function $\Phi(\xi, k_T, \mu)$ is needed to describe the parton distribution not only in the momentum fraction ξ, but also in the transverse momentum k_T. The DIS cross section is then written, in the k_T factorization theorem, as the convolution

$$F_2(x, Q^2) = \sum_f \int_x^1 \frac{d\xi}{\xi} \int d^2 k_T H_f(x/\xi, k_T, Q, \mu) \Phi_{f/N}(\xi, k_T, \mu). \tag{34}$$

The k_T factorization theorem is also applicable to the analysis of low p_T spectra of final states, like direct photon and jet productions, for which $k_T \sim p_T$ is not negligible.

A collinear gluon emission, modifying a parton longitudinal momentum, generates a parton transverse momentum k_T at the same time. The factorization of a TMD from the DIS is similar to that of a PDF, which relies on the eikonal approximation in the collinear region. This procedure results in the

eikonal propagator $n_-^\nu / n_- \cdot l$, represented by the Wilson lines similar to that defined in Eq. (24). A naive TMD definition as an extension of the PDF in Eq. (23) is given by

$$
\begin{aligned}
\Phi_{q/N}(\xi, k_T, \mu) &= \int \frac{dy^-}{2\pi} \int \frac{d^2 y_T}{(2\pi)^2} e^{-i\xi p^+ y^- + i\mathbf{k}_T \cdot \mathbf{y}_T} \\
&\times \frac{1}{2} \langle N(p,\sigma) | \bar{q}(0, y^-, y_T) \frac{1}{2} \gamma^+ W(y^-, y_T, 0, 0_T) q(0, 0, 0_T) | N(p, \sigma) \rangle, \quad (35)
\end{aligned}
$$

with the Wilson links $W(y^-, y_T, 0, 0_T) = W(0, 0_T) I_{0,y_T} W^\dagger(y^-, y_T)$. Because the valence quark fields before and after the final-state cut are separated by a transverse distance in this case, the vertical links I_{0,y_T} located at $y^- = \infty$ are demanded by the gauge invariance of a TMD [32]. More investigations on the vertical Wilson links can be found in [33].

Though we do need the k_T factorization theorem, many of its aspects have not yet been completely understood. For example, the naive definition in Eq. (35) is actually ill-defined, due to the existence of the light-cone singularity, that arises from a loop momentum parallel to the Wilson line direction n_-. A plausible modification is to rotate the Wilson line away from the light cone, namely, to replace n_- by a vector n with $n^2 \neq 0$. This rotation is allowed, since the collinear divergences are insensitive to the direction n as illustrated in Eq. (26) [34]: even when n_- is rotated to n, only the minus component n^- is relevant for the evaluation of the collinear divergences. A detailed discussion on this subtle issue can be found in [35]. Besides, a parton is off-shell by $-k_T^2$, once k_T is retained. Then whether a hard kernel obtained in the k_T factorization theorem is gauge invariant becomes a concern [36]. Dropping the k_T dependence of the hard kernel in Eq. (34), the integration of the TMD over k_T, $\int d^2 k_T \Phi_{f/N}(\xi, k_T)$, can be worked out. How this integral is related to the PDF $\phi_{f/N}(\xi)$ in Eq. (23) is worth of a thorough study.

3 Evolution and resummation

As stated in the previous section, radiative corrections in pQCD produce large logarithms at each order of the coupling constant. Double logarithms appear in processes involving two scales, such as $\ln^2(p^+ b)$ with p^+ being the large longitudinal momentum of a parton and $1/b$ being the small inverse impact parameter, where b is conjugate to the parton transverse momentum k_T. In the region with large Bjorken variable x, there exists $\ln^2(1/N)$ from the Mellin transformation of $\ln(1-x)/(1-x)_+$, for which the two scales are the large p^+ and the small infrared cutoff $(1-x)p^+$ for gluon emissions from a parton. Single logarithms are generated in processes involving one scale, such as $\ln p^+$ and $\ln(1/x)$, for which the relevant scales are the large p^+ and the small xp^+, respectively. Various methods have been developed to organize these logarithmic corrections to a PDF or a TMD: the k_T resummation for $\ln^2(p^+ b)$ [8,9], the threshold resummation for $\ln^2(1/N)$ [5–7], the joint resummation [11,12] that unifies the above two formalisms, the DGLAP equation for $\ln p^+$ [3], the BFKL equation for $\ln(1/x)$ [4], and the CCFM equation [10] that combines the above two evolution equations. I will explain the basic ideas of all the single- and double-logarithmic summations in the Collins-Soper-Sterman (CSS) resummation formalism [8,9].

3.1 Resummation Formalism

Collinear and soft divergences may overlap to form double logarithms in extreme kinematic regions, such as low p_T and large x. The former includes low p_T jet, photon, and W boson productions, which all require real gluon emissions with small p_T. The latter includes top pair production, DIS, DY production, and heavy meson decays $B \to X_u l\nu$ and $B \to X_s \gamma$ [16, 37, 38] at the end points, for which parton momenta remain large, and radiations are constrained in the soft region. Because of the limited phase space for real gluon corrections, the infrared cancellation is not complete. The double logarithms, appearing in products with the coupling constant α_s, such as $\alpha_s \ln^2(E/p_T)$ with the beam energy E and $\alpha_s \ln(1-x)/(1-x)_+$, deteriorate perturbative expansion. Double logarithms also occur in exclusive
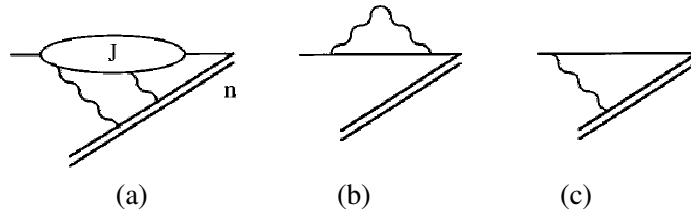
Fig. 4: (a) Jet subprocess defined in Eq. (36). (b) and (c) LO diagrams of (a).

Fig. 5: Derivative $p^+ dJ/dp^+$ in the covariant gauge.

processes, such as Landshoff scattering [39], hadron form factors [40], Compton scattering [41] and heavy-to-light transitions $B \to \pi(\rho)$ [42] and $B \to D^{(*)}$ [43] at maximal recoil. In order to have a reliable pQCD analysis of these processes, the important logarithms must be summed to all orders.

The resummation of large logarithms will be demonstrated in the covariant gauge $\partial \cdot A = 0$ [38], in which the role of the Wilson line direction n and the key technique can be explained straightforwardly. Take as an example a jet subprocess defined by the matrix element

$$J(p,n)u(p) = \langle 0 | \mathcal{P} \exp\left[-ig \int_0^\infty dz\, n \cdot A(nz)\right] q(0) | p \rangle \ , \tag{36}$$

where q is a light quark field with momentum p, and $u(p)$ is a spinor. The abelian case of this subprocess has been discussed in [44]. The path-ordered exponential in Eq. (36) is the consequence of the factorization of collinear gluons with momenta parallel to p from a full process, as explained in the previous section. For convenience, it is assumed that p has a large light-cone component p^+, and all its other components vanish. A general diagram of the jet function J is shown in Fig. 4(a), where the path-ordered exponential is represented by a double line along the vector n. As explained before, varying the direction n does not change the collinear divergences collected by the Wilson line.

It is easy to see that J contains double logarithms from the overlap of collinear and soft divergences by calculating the LO diagrams in Fig. 4(b), the self-energy correction, and in Fig. 4(c), the vertex correction. In the covariant gauge both Figs. 4(b) and 4(c) produce double logarithms. In the axial gauge $n \cdot A = 0$ the path-ordered exponential reduces to an identity, and Fig. 4(c) does not exist. The essential step in the resummation technique is to derive a differential equation $p^+ dJ/dp^+ = CJ$ [16, 38, 42], where the coefficient function C contains only single logarithms, and can be treated by RG methods. Since the path-ordered exponential is scale-invariant in n, J must depend on p and n through the ratio $(p \cdot n)^2/n^2$. The differential operator d/dp^+ can then be replaced by d/dn using a chain rule

$$p^+ \frac{d}{dp^+} J = -\frac{n^2}{v \cdot n} v_\alpha \frac{d}{dn_\alpha} J, \tag{37}$$

with the vector $v = (1, 0, \mathbf{0}_T)$ being defined via $p = p^+ v$.

Equation (37) simplifies the analysis tremendously, because n appears only in the Feynman rules for the Wilson line, while p may flow through the whole diagram in Fig. 4(a). The differentiation of each eikonal vertex and of the associated eikonal propagator with respect to n_α,

$$-\frac{n^2}{v \cdot n} v_\alpha \frac{d}{dn_\alpha} \frac{n_\mu}{n \cdot l} = \frac{n^2}{v \cdot n} \left(\frac{v \cdot l}{n \cdot l} n_\mu - v_\mu \right) \frac{1}{n \cdot l} \equiv \frac{\hat{n}_\mu}{n \cdot l}, \tag{38}$$
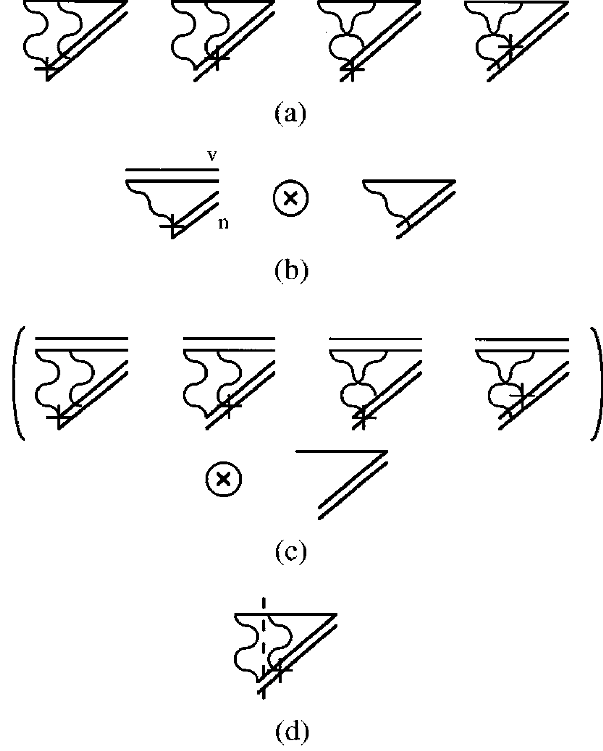
(a)

(b)

(c)

(d)

Fig. 6: (a) $O(\alpha_s^2)$ examples for the differentiated J. (b) Factorization of K at $O(\alpha_s)$. (c) Factorization of K at $O(\alpha_s^2)$. (d) Factorization of G at $O(\alpha_s)$.

leads to the special vertex $\hat{n}_\mu$. The derivative $p^+ dJ/dp^+$ is thus expressed as a summation over different attachments of $\hat{n}_\mu$, labeled by the symbol $+$ in Fig. 5. If the loop momentum l is parallel to p, the factor $v \cdot l$ vanishes, and $\hat{n}_\mu$ is proportional to v_μ. When this $\hat{n}_\mu$ is contracted with a vertex in J, in which all momenta are mainly parallel to p, the contribution to $p^+ dJ/dp^+$ is suppressed. Therefore, the leading regions of l are soft and hard.

According to this observation, we investigate some two-loop examples exhibited in Fig. 6(a). If the loop momentum flowing through the special vertex is soft but another is not, only the first diagram is important, giving a large single logarithm. In this soft region the subdiagram containing the special vertex can be factorized using the eikonal approximation as shown in Fig. 6(b), where the symbol $\otimes$ represents a convoluting relation. The subdiagram is absorbed into a soft kernel K, and the remainder is identified as the original jet function J, both being $O(\alpha_s)$ contributions. If both the loop momenta are soft, the four diagrams in Fig. 6(a) are equally important. The subdiagrams, factorized according to Fig. 6(c), contribute to K at $O(\alpha_s^2)$, and the remainder is the LO diagram of J. If the loop momentum flowing through the special vertex is hard and another is not, the second diagram in Fig. 6(a) dominates. In this region the subdiagram containing the special vertex is factorized as shown in Fig. 6(d). The right-hand side of the dashed line is absorbed into a hard kernel G as an $O(\alpha_s)$ contribution, and the left-hand side is identified as the $O(\alpha_s)$ diagram of J. If both the loop momenta are hard, all the diagrams in Fig. 6(a) are absorbed into G, giving the $O(\alpha_s^2)$ contributions.

Extending the above reasoning to all orders, one derives the differential equation

$$p^+ \frac{d}{dp^+} J = \left[K(m/\mu, \alpha_s(\mu)) + G(p^+\nu/\mu, \alpha_s(\mu)) \right] J, \qquad (39)$$

where the coefficient function C has been written as the sum of the soft kernel K and the hard kernel G. In the above expression μ is a factorization scale, the gauge factor in G is defined as $\nu = \sqrt{(v \cdot n)^2/|n^2|}$,

and a gluon mass m has been introduced to regularize the infrared divergence in K. It has been made explicit that K and G depend on a single infrared scale m and a single ultraviolet scale p^+, respectively.

The $O(\alpha_s)$ contribution to K from Fig. 6(b) is written as

$$K = -ig^2 C_F \mu^\epsilon \int \frac{d^{4-\epsilon}l}{(2\pi)^{4-\epsilon}} \frac{\hat{n}_\mu}{n \cdot l} \frac{g^{\mu\nu}}{l^2 - m^2} \frac{v_\nu}{v \cdot l} - \delta K, \tag{40}$$

δK being an additive counterterm. The $O(\alpha_s)$ contribution to G from Fig. 6(d) is given by

$$G = -ig^2 C_F \mu^\epsilon \int \frac{d^{4-\epsilon}l}{(2\pi)^{4-\epsilon}} \frac{\hat{n}_\mu}{n \cdot l} \frac{g^{\mu\nu}}{l^2} \left(\frac{\not{p} + \not{l}}{(p+l)^2} \gamma_\nu - \frac{v_\nu}{v \cdot l} \right) - \delta G, \tag{41}$$

where the second term in the parentheses acts as a soft subtraction to avoid double counting, and δG is an additive counterterm. A straightforward evaluation shows that Eqs. (40) and (41) contain only the single logarithms $\ln(m/\mu)$ and $\ln(p^+\nu/\mu)$, respectively, as claimed before. Organizing these single logarithms using RG methods, and then solving Eq. (39), one resums the double logarithms $\ln^2(p^+/m)$ in J.

To explain all the known resummations and evolution equations, we first construct a master equation for the TMD $\Phi(x, k_T)$, which is a differential equation in the hadron momentum p^+. The dependence on the factorization scale μ is implicit. If the parton is a quark, Φ is defined by Eq. (35). If the parton is a gluon, the nonlocal operator in the hadronic matrix element of Eq. (35) is replaced by $F_\mu^+(y^-, y_T)F^{\mu+}(0)$. Similarly, n is varied arbitrarily away from the light cone with $n^2 \neq 0$. Then Φ depends on p^+ via the ratio $(p \cdot n)^2/n^2$, so the chain rule in Eq. (37) relating the derivative $d\Phi/dp^+$ to $d\Phi/dn_\alpha$ applies. Following the derivation in the previous subsection, one obtains the master equation

$$p^+ \frac{d}{dp^+} \Phi(x, k_T) = 2\bar{\bar{\Phi}}(x, k_T), \tag{42}$$

where $\bar{\bar{\Phi}}$ contains the special vertex, and the coefficient 2 is attributed to the equality of $\bar{\bar{\Phi}}$ with the special vertex on either side of the final-state cut.

The function $\bar{\bar{\Phi}}$ is factorized into the convolution of the soft and hard kernels with Φ:

$$\bar{\bar{\Phi}}(x, k_T) = \bar{\bar{\Phi}}_s(x, k_T) + \bar{\bar{\Phi}}_h(x, k_T), \tag{43}$$

with the soft contribution

$$\begin{aligned}
\bar{\bar{\Phi}}_s &= \left[-ig^2 C_F \mu^\epsilon \int \frac{d^{4-\epsilon}l}{(2\pi)^{4-\epsilon}} \frac{\hat{n} \cdot v}{n \cdot l \, l^2 v \cdot l} - \delta K \right] \Phi(x, k_T) \\
&\quad -ig^2 C_F \mu^\epsilon \int \frac{d^{4-\epsilon}l}{(2\pi)^{4-\epsilon}} \frac{\hat{n} \cdot v}{n \cdot l \, v \cdot l} 2\pi i \delta(l^2) \Phi(x + l^+/p^+, |\mathbf{k}_T + \mathbf{l}_T|),
\end{aligned} \tag{44}$$

where the first term is the same as in Eq. (40), and the second term proportional to $\delta(l^2)$ arises from the real soft gluon emission. The hard contribution is given by $\bar{\bar{\Phi}}_h(x, k_T) = G(xp^+\nu/\mu, \alpha_s(\mu))\Phi(x, k_T)$, in which the hard kernel G is the same as in Eq. (41).

3.2 k_T Resummation and BFKL Equation

The TMD definition in Eq. (35) contains three scales: $(1 - x)p^+$, xp^+, and k_T. We first consider the soft approximation corresponding to the rapidity ordering of real gluon emissions in a ladder diagram. Assume that a parton carries the longitudinal momentum $xp^+ + l_2^+ + l_1^+$, which becomes $xp^+ + l_1^+$ after emitting a gluon of longitudinal momentum l_2^+ and transverse momentum l_{2T}, and then becomes xp^+ after emitting a gluon of longitudinal momentum l_1^+ and transverse momentum l_{1T}. In the kinematic configuration with $l_2^+ \gg l_1^+$ and $l_{2T} \sim l_{1T}$, the original parton momentum is approximated by $xp^+ + l_2^+ + l_1^+ \approx xp^+ + l_2^+$. The loop integral associated with the first gluon emission is then independent
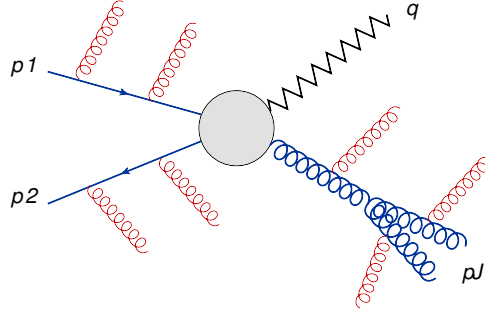
Fig. 7: Scattering amplitude for direct photon production.

of l_1^+, and can be worked out straightforwardly, giving a logarithm. The loop integral associated with the second gluon emission, involving only l_1^+, also gives a logarithm. Therefore, a ladder diagram with N rung gluons generates the logarithmic correction $(\alpha_s L)^N$ under the above rapidity ordering, where L denotes the large logarithm. Following the rapidity ordering, we adopt the approximation for the real gluon emission in Eq. (44)

$$\Phi(x + l^+/p^+, |\mathbf{k_T} + \mathbf{l_T}|) \approx \Phi(x, |\mathbf{k_T} + \mathbf{l_T}|), \tag{45}$$

where the l^+ dependence has been neglected. The transverse momenta l_T, being of the same order as k_T in this kinematic configuration, is kept. The variable l^+ in K is then integrated up to infinity, such that the scale $(1-x)p^+$ disappears.

Equation (44) is Fourier transformed into the impact parameter b space to decouple the l_T integration. Hence, in the intermediate x region Φ involves two scales, the large xp^+ that characterizes the hard kernel G and the small $1/b$ that characterizes the soft kernel K. The master equation (42) becomes

$$p^+ \frac{d}{dp^+}\Phi(x,b) = 2\left[K(1/(b\mu), \alpha_s(\mu)) + G(xp^+\nu/\mu, \alpha_s(\mu))\right]\Phi(x,b), \tag{46}$$

whose solution with $\nu = 1$ leads to the k_T resummation

$$\Phi(x,b) = \Delta_k(x,b)\Phi_i(x), \tag{47}$$

with the Sudakov exponential

$$\Delta_k(x,b) = \exp\left[-2\int_{1/b}^{xp^+}\frac{dp}{p}\int_{1/b}^{p}\frac{d\mu}{\mu}\gamma_K(\alpha_s(\mu))\right], \tag{48}$$

and the initial condition Φ_i of the Sudakov evolution. The anomalous dimension of K, $\lambda_K = \mu d\delta K/d\mu$, is given, up to two loops, by [45]

$$\gamma_K = \frac{\alpha_s}{\pi}C_F + \left(\frac{\alpha_s}{\pi}\right)^2 C_F\left[C_A\left(\frac{67}{36} - \frac{\pi^2}{12}\right) - \frac{5}{18}n_f\right], \tag{49}$$

with n_f being the number of quark flavors and $C_A = 3$ being a color factor.

The k_T resummation effect on the low p_T spectra of the direct photon production depicted in Fig. (7) has been analyzed [46]. The initial-state and final-state radiations are constrained in the low p_T region, where the k_T resummation is necessary for improving the perturbation theory. Figure 8 shows the deviation (Data -Theory)/Theory of the NLO pQCD predictions, obtained using the CTEQ4M PDFs [47], from the experimental data as a function of $x_t = 2p_T/\sqrt{s}$, $\sqrt{s}$ being the center-of-mass energy. The deviation is huge as expected, especially at low x_t of each set of the data. After including
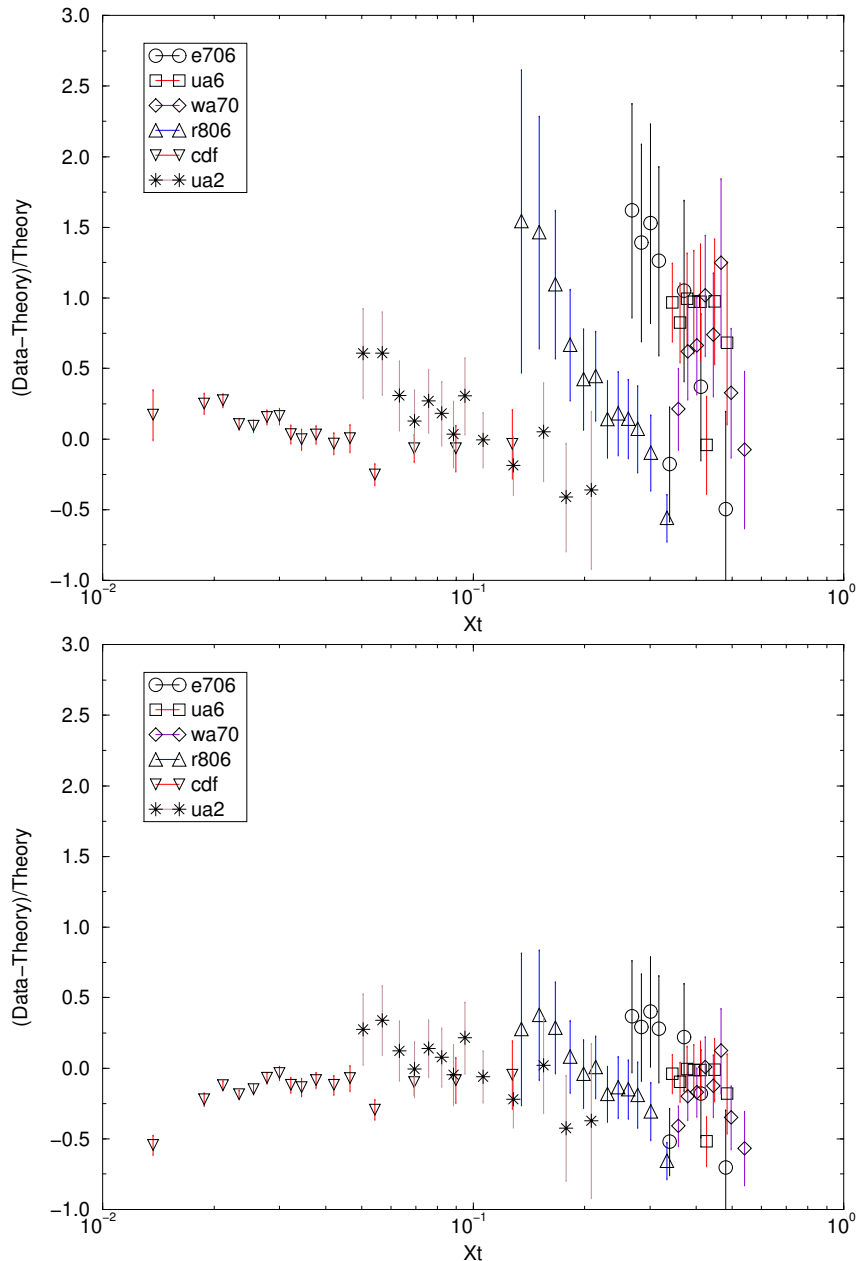
Fig. 8: Low p_T direct photon spectra before (upper) and after (lower) including the k_T resummation.

the k_T resummation effect [46], it is clear that a significant improvement on the agreement between theoretical predictions and the data is achieved. As to the intermediate- and high-p_T regions of the direct photon production, NLO pQCD works reasonably well in accommodating the data as indicated in Fig. 9. The threshold resummation effect, which will be introduced in the next subsection, is more relevant in these regions: it slightly improves the consistency between predictions and the data [48].

In the small x region with $xp^+ \sim k_T$, or $xp^+ \sim 1/b$ in the b space, the two-scale case reduces to the single-scale one. In this region contributions from gluonic partons dominate, so Φ represents the gluon TMD below. The source of double logarithms, i.e., the integral containing the anomalous dimension γ_K, is less important. Because only the soft scale exists, one drops the hard kernel G, and keeps the soft kernel with an ultraviolet cutoff. The right-hand side of Eq. (42) becomes

$$\bar{\Phi}(x, k_T) = -ig^2 N_c \int \frac{d^4 l}{(2\pi)^4} \frac{\hat{n} \cdot v}{n \cdot l v \cdot l} \left[\frac{\theta(k_T^2 - l_T^2)}{l^2} \Phi(x, k_T) \right.$$
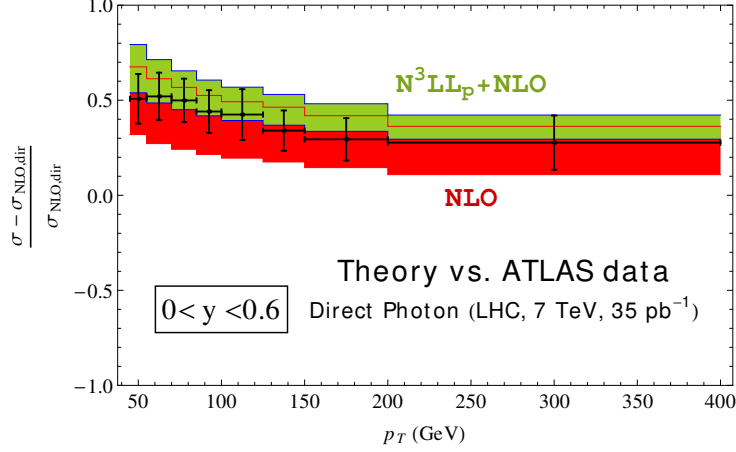
Fig. 9: High p_T direct photon spectrum under the threshold resummation.

$$+2\pi i\delta(l^2)\phi(x,|\mathbf{k}_T + \mathbf{l}_T|)\big]\,, \tag{50}$$

where the color factor C_F has been replaced by N_c for the gluon TMD. The θ function introduces the ultraviolet cutoff on l_T mentioned above. To make variation in x via variation in p^+, a fixed parton momentum is assumed. Under this assumption, the momentum fraction x is proportional to $1/p^+$, and one has $p^+d\Phi/dp^+ = -xd\Phi/dx\Phi$ [49]. Performing the integrations over l^+ and l^- in Eq. (50), the master equation (42) reduces to the BFKL equation [50],

$$\frac{d\phi(x,k_T)}{d\ln(1/x)} = \bar{\alpha}_s \int \frac{d^2 l_T}{\pi l_T^2} \left[\phi(x,|\mathbf{k}_T + \mathbf{l}_T|) - \theta(k_T^2 - l_T^2)\phi(x,k_T)\right]\,, \tag{51}$$

with the coupling constant $\bar{\alpha}_s = N_c\alpha_s/\pi$.

A remarkable prediction of the above LO BFKL equation is that a high-energy cross section increases with the center-of-mass energy,

$$\sigma \approx \frac{1}{t}\left(\frac{s}{t}\right)^{\omega_P - 1}\,, \tag{52}$$

with the momentum transfer squared t. It turns out that Eq. (52), with the Pomeron intercept $\omega_P - 1 = 4\bar{\alpha}_s \ln 2$, violates the Froissart (unitarity) bound $\sigma < \text{const.} \times \ln^2$ [51]. The unsatisfactory prediction of the LO BFKL equation called for the NLO corrections [52], which were, however, found to be dramatic as indicated by the x dependence of the derivative of the structure function $dF_L/d\ln Q^2$ in Fig. 10 [53]: the NLO effect is nearly as large as the LO result for $x \sim 0.001$, and becomes dominant at lower x. It even turns $dF_L/d\ln Q^2$ negative below $x \sim 0.0001$ in the upper of Fig. 10. That is, the perturbative solution is not at all stable. Choosing a running coupling constant [53], the NLO effect is not overwhelming, but still significant as exhibited in the lower of Fig. 10.

3.3 Threshold Resummation and DGLAP Equation

We then consider the soft approximation corresponding to the k_T ordering of real gluon emissions in a ladder diagram. Assume that a parton without the transverse momentum, carries $-\mathbf{l}_{1T}$ after emitting a gluon of longitudinal momentum l_1^+ and transverse momentum $\mathbf{l}_{1T}$, and then carries $-\mathbf{l}_{1T} - \mathbf{l}_{2T}$ after emitting a gluon of longitudinal momentum l_2^+ and transverse momentum $\mathbf{l}_{2T}$. In the kinematic configuration with $l_{2T} \gg l_{1T}$ and $l_2^+ \sim l_1^+$, the final parton momentum can be approximated by $-\mathbf{l}_{2T} - \mathbf{l}_{1T} \approx -\mathbf{l}_{2T}$, such that the loop integral associated with the first gluon emission involves only
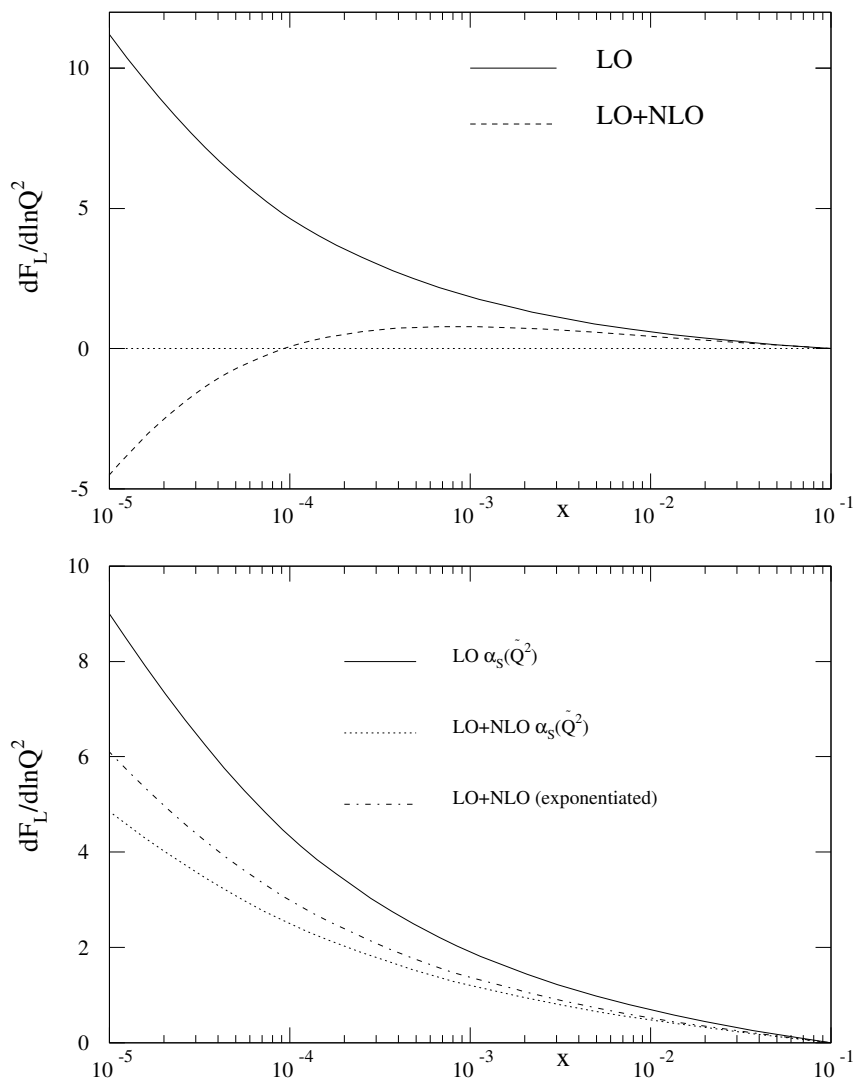
Evolution of F_L, $\ln(Q^2/\Lambda^2)=8$, $F_L=(x/0.1)^{-0.3}$

Fig. 10: Effects from LO and NLO BFKL equations.

l_{1T}, and can be worked out straightforwardly, giving a logarithm. The loop integral associated with the second gluon emission involves only l_{2T}, and also gives a logarithm. Hence, a ladder diagram with N rung gluons generates the logarithmic correction $(\alpha_s L)^N$ under the above k_T ordering. In this case Φ is independent of l_T, and we have the approximation for the real gluon emission in Eq. (44)

$$\Phi(x + l^+/p^+, |\mathbf{k_T} + \mathbf{l_T}|) \approx \Phi(x + l^+/p^+, k_T), \tag{53}$$

in which x and l^+/p^+ are of the same order. The dependence on k_T can then be integrated out from both sides of the master equation (42), and the TMD Φ reduces to the PDF ϕ. The scale k_T disappears, and the scale $(1-x)p^+$ is retained.

The Mellin transformation is employed to bring $\bar{\phi}_s$ from the momentum fraction x space to the moment N space,

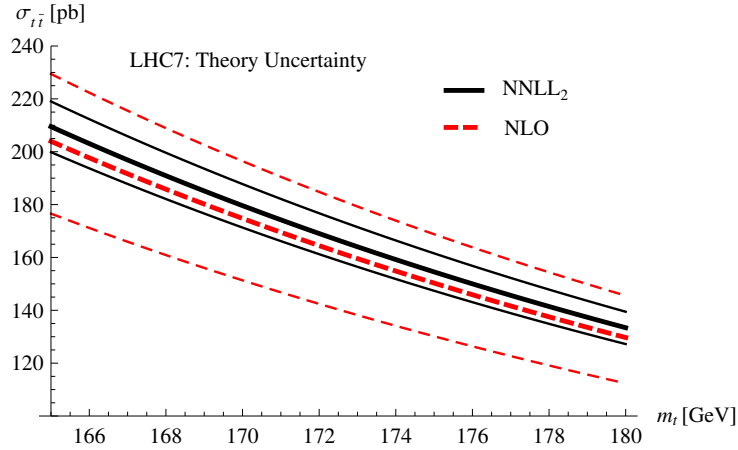$$\bar{\phi}_s(N) \quad = \quad \int_0^1 dx\, x^{N-1} \bar{\phi}_s(x), \tag{54}$$

Fig. 11: Dependence of the total cross section for the top-pair production on the top mass at the LHC with $\sqrt{s} = 7$ TeV.

under which the l^+ integration decouples. In the large x region ϕ involves two scales, the large $xp^+ \sim p^+$ from the hard kernel G and the small $(1-x)p^+ \sim p^+/N$ from the soft kernel K. To sum $\ln(1/N)$, we rewrite the derivative $p^+ d\phi/dp^+$ as

$$p^+ \frac{d\phi}{dp^+} = \frac{p^+}{N} \frac{d\phi}{d(p^+/N)}. \tag{55}$$

The solution of the master equation (42) then gives the threshold resummation,

$$\phi(N) = \Delta_t(N)\phi_i \tag{56}$$

with the exponential

$$\Delta_t(N) = \exp\left[-2 \int_{p^+/N}^{p^+} \frac{dp}{p} \int_{p^+}^{p} \frac{d\mu}{\mu} \gamma_K(\alpha_s(\mu))\right], \tag{57}$$

or its equivalent expression

$$\Delta_t(N) = \exp\left[\int_0^1 dz \frac{1-z^{N-1}}{1-z} \int_{(1-z)^2}^1 \frac{d\lambda}{\lambda} \gamma_K(\alpha_s(\sqrt{\lambda}p^+))\right]. \tag{58}$$

An application of the threshold resummation is found in the analysis of the top-quark pair production, which was performed at the next-to-next-to-leading-logarithmic (NNLL) accuracy [54]. It has been observed that the threshold resummation effect enhances the NLO total cross section by few percents as shown in Fig. 11, where the bands sandwiched by the thinner lines denote the theory uncertainty. The above formalism can be used to determine of the top quark mass as indicated in Fig. 12, where the solid lines represent the central values, and the total uncertainties of the theoretical and experimental results [55] are given by the external dashed lines.

In the intermediate x region the two-scale case reduces to the single-scale one because of $xp^+ \sim (1-x)p^+$, and the source of double logarithms is less important. Without the Mellin transformation, the sum in Eq. (43), with the approximation in Eq. (53) being inserted, leads to the DGLAP equation [49],

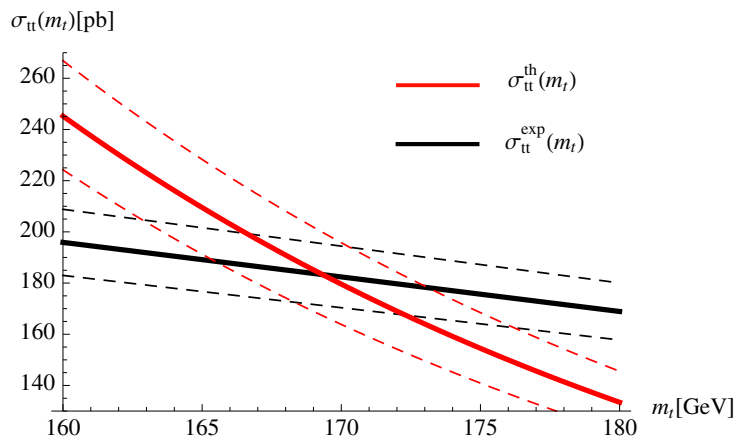$$p^+ \frac{d}{dp^+} \phi(x) = \int_x^1 \frac{d\xi}{\xi} P(x/\xi)\phi(\xi), \tag{59}$$

Fig. 12: Mass dependence of the theoretical cross section with the threshold resummation effect (red) and of the measured cross section (black).
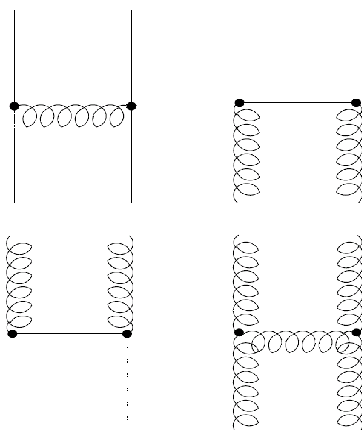

Fig. 13: Diagrams for the DGLAP splitting functions.

with the kernel

$$P(z) = \frac{\alpha_s(p^+)}{\pi} C_F \frac{2}{(1-z)_+} ,\tag{60}$$

where the variable change $\xi = x + l^+/p^+$ has been made. The argument of α_s, i.e, the factorization scale μ, has been set to the scale $xp^+ \sim (1-x)p^+ \sim O(p^+)$. Note that the kernel P differs from the splitting function P_{qq} in Eq. (22) by the term $(z^2 - 1)/(1-z)_+$, which is finite in the $z \to 1$ limit. The reason is that the real gluon emission was evaluated under the soft approximation as deriving P, while it was calculated exactly as deriving P_{qq}.

Gluon emissions in Fig. 13 cause the mixing between the quark and gluon PDFs, giving the complete set of DGLAP equations with four splitting functions

$$\frac{\partial}{\partial \ln Q^2} \begin{pmatrix} \phi_q \\ \phi_g \end{pmatrix} = \begin{pmatrix} P_{qq} & P_{qg} \\ P_{gq} & P_{gg} \end{pmatrix} \otimes \begin{pmatrix} \phi_q \\ \phi_g \end{pmatrix}.\tag{61}$$

The evolution of the u-quark and d-quark PDFs in Q^2 predicted by the LO DGLAP equation [56] is shown in Fig. 14, where the inputs at the initial scale $Q_0 = 1$ GeV were taken from MRST2001 [57]. It is observed that the valence quark PDFs increase with Q^2 at small x, namely, they become broader with Q^2, a feature consistent with what was stated in the previous section. The predictions for the
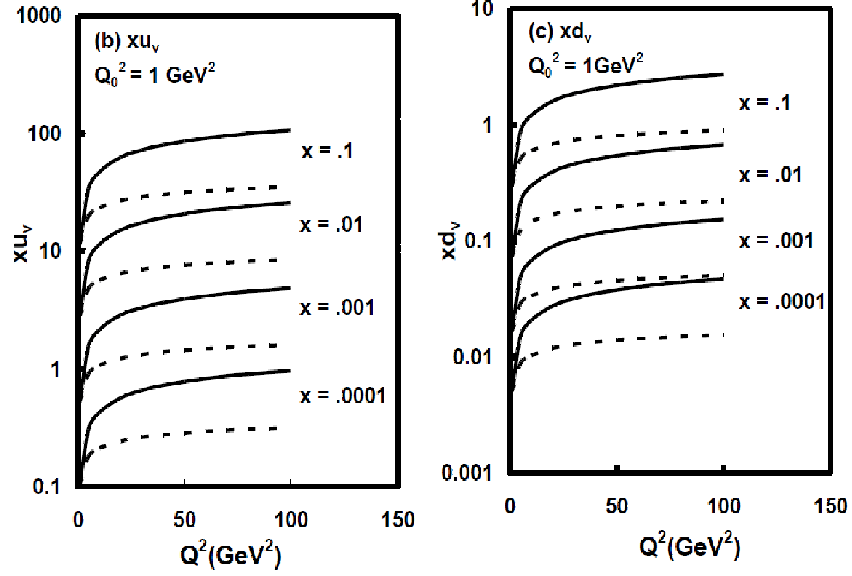
Fig. 14: Q^2 evolutions of the valence quark PDFs for some parameter values in the DGLAP solutions (solid and dashed lines).
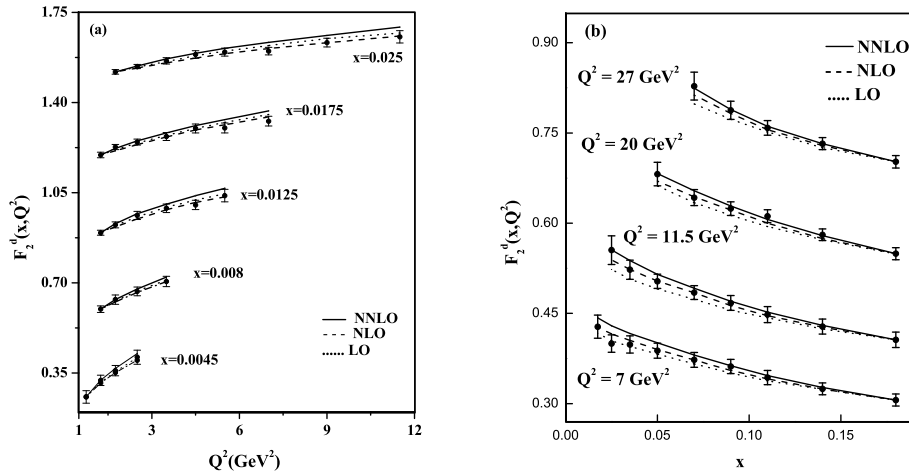

Fig. 15: Predictions from the DGLAP equation and the NMC data for the deuteron structure function. For clarity, data are scaled up by +0.2i (in Fig.(a)) and +i (in Fig.(b)) (with i = 0,1,2,3) starting from the bottom of the graphs.

deuteron structure function derived from the LO, NLO, and NNLO DGLAP equations are displayed in Fig. 15 [58], which agree with the NMC data [59].

3.4   Joint Resummation and CCFM Equation

At last, a unified resummation formalism for large and intermediate x and a unified evolution equation for intermediate and small x can be derived by retaining the l^+ and l_T dependencies of Φ in Eq. (44), which corresponds to the so-called angular ordering. In this case both the Fourier and Mellin transformations are applied to Eq. (44), leading to

$$\bar{\Phi}_s(N, b) = K(p^+/(N\mu), 1/(b\mu), \alpha_s(\mu))\Phi(N, b) \,, \tag{62}$$

with the soft kernel [11]

$$
\begin{aligned}
K &= -ig^2 C_F \mu^\epsilon \int_0^1 dz \int \frac{d^{4-\epsilon}l}{(2\pi)^{4-\epsilon}} \frac{\hat{n} \cdot v}{n \cdot l v \cdot l} \left[\frac{\delta(1-z)}{l^2} \right. \\
&\quad \left. + 2\pi i \delta(l^2) \delta\left(1 - z - \frac{l^+}{p^+}\right) z^{N-1} e^{i\mathbf{l}_T \cdot \mathbf{b}} \right] - \delta K, \\
&= \frac{\alpha_s(\mu)}{\pi} C_F \left[\ln \frac{1}{b\mu} - K_0\left(\frac{2\nu p^+ b}{N}\right) \right],
\end{aligned}
\tag{63}
$$

K_0 being the modified Bessel function. As $p^+ b \gg N$, we have $K_0 \to 0$, and the soft scale inferred by the above expression approaches $1/b$ for the k_T resummation. As $N \gg p^+ b$, we have $K_0 \approx -\ln(\nu p^+ b/N)$, and the soft scale approaches p^+/N for the threshold resummation.

Following the procedures similar to Eqs. (46)-(48), we derive the joint resummation

$$
\Phi(N, b) = \Delta_u(N, b)\Phi_i,
\tag{64}
$$

with the exponential

$$
\Delta_u(N, b) = \exp\left[-2 \int_{p^+\chi^{-1}(N,b)}^{p^+} \frac{dp}{p} \int_{p^+\chi^{-1}(1,b)}^{p} \frac{d\mu}{\mu} \gamma_K(\alpha_s(\mu)) \right].
\tag{65}
$$

The dimensionless function [12]

$$
\chi(N, b) = \left(N + \frac{p^+ b}{2} \right) e^{\gamma_E},
\tag{66}
$$

is motivated by the limits discussed above. It is apparent that Eq. (65) reduces to Eq. (48) and Eq. (57) in the $b \to \infty$ and $N \to \infty$ limits, respectively. The effect from the joint resummation on the q_T spectra of selectron pairs produced at the LHC with $\sqrt{S} = 14$ TeV has been investigated in [60]. It is seen in Fig. 16 that the joint and k_T resumations exhibit a similar behavior in the small-q_T region as expected, but the jointly-resummed cross section is about 5%-10% lower than the k_T-resummed cross section in the range 50 GeV $< q_T <$ 100 GeV.

In the intermediate and small x regions, it is not necessary to resum the double logarithms $\ln^2(1/N)$. After extracting the k_T resummation, the remaining single-logarithmic summation corresponds to a unification of the DGLAP and BFKL equations, since both the l^+ and l_T dependencies have been retained. The function $\Phi(x + l^+/p^+, b)$ in Eq. (44) is reexpressed, after the Fourier transformation, as

$$
\begin{aligned}
\Phi(x + l^+/p^+, b) &= \theta((1-x)p^+ - l^+)\Phi(x, b) \\
&\quad + [\Phi(x + l^+/p^+, b) - \theta((1-x)p^+ - l^+)\Phi(x, b)].
\end{aligned}
\tag{67}
$$

The contribution from the first term is combined with the first term in Eq. (44), giving the soft kernel K for the k_T resummation. The second term in Eq. (67) contributes

$$
-iN_c g^2 \int \frac{d^4 l}{(2\pi)^4} \frac{\hat{n} \cdot v}{n \cdot l v \cdot l} 2\pi i \delta(l^2) e^{i\mathbf{l}_T \cdot \mathbf{b}} [\Phi(x + l^+/p^+, b) - \theta((1-x)p^+ - l^+)\Phi(x, b)],
\tag{68}
$$

which will generate the splitting function below. The color factor has been replaced by N_c, since the gluon TMD is considered here.

The master equation (42) then becomes

$$
p^+ \frac{d}{dp^+} \Phi(x, b) = -2 \left[\int_{1/b}^{xp^+} \frac{d\mu}{\mu} \gamma_K(\alpha_s(\mu)) - \bar{\alpha}_s(xp^+) \ln(p^+ b) \right] \Phi(x, b)
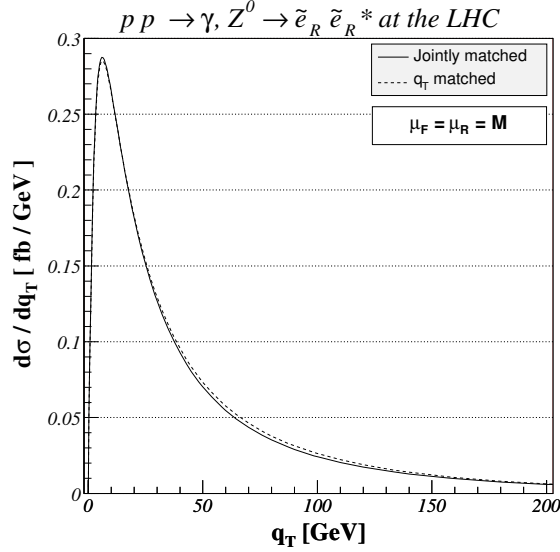$$

Fig. 16: Transverse-momentum distribution of selectron pairs at the LHC in the framework of joint (full) and k_T (dotted) resummations.

$$+2\bar{\alpha}_s(xp^+) \int_x^1 dz P_{gg}(z) \Phi(x/z, b), \tag{69}$$

with the splitting function

$$P_{gg} = \left[\frac{1}{(1-z)_+} + \frac{1}{z} - 2 + z(1-z) \right], \tag{70}$$

obtained from Eq. (68). The term $-2 + z(1-z)$ finite as $z \to 0$ and $z \to 1$ has been added. The exponential Δ is extracted from the k_T resummation,

$$\Delta(x, b, Q_0) = \exp \left(-2 \int_{xQ_0}^{xp^+} \frac{dp}{p} \left[\int_{1/b}^{p} \frac{d\mu}{\mu} \gamma_K(\alpha_s(\mu)) - \bar{\alpha}_s(p) \ln \frac{pb}{x} \right] \right), \tag{71}$$

Q_0 being an arbitrary low energy scale. It is trivial to justify by substitution that the solution is given by

$$
\begin{aligned}
\Phi(x, b) &= \Delta(x, b, Q_0)\Phi_i \\
&+ 2 \int_x^1 dz \int_{Q_0}^{p^+} \frac{d\mu}{\mu} \bar{\alpha}_s(x\mu) \Delta_k(x, b) P_{gg}(z) \Phi(x/z, b),
\end{aligned}
\tag{72}
$$

which can be regarded as a modified version of the CCFM equation [10].

4 PQCD for jet physics

Jets, abundantly produced at colliders [61], carry information of hard scattering and parent particles, which is crucial for particle identification and new physics search. Study of jet physics is usually done using event generators, which, however, suffer ambiguity from parameter tuning. Hence, we are motivated to establish an alternative approach free of the ambiguity. I will demonstrate that jet dynamics can be explored and jet properties can be predicted in the pQCD resummation formalism.

We start from the dijet production in the e^-e^+ annihilation, which is part of its total cross section. The physical dijet final state, described in Fig. 17, contains two jet cones of half angle δ and isotropic soft gluons within the energy resolution ϵQ, Q being the e^-e^+ invariant mass. The Born cross section is the same as the total one in Eq. (11). With the constrained phase space for real gluons, the infrared
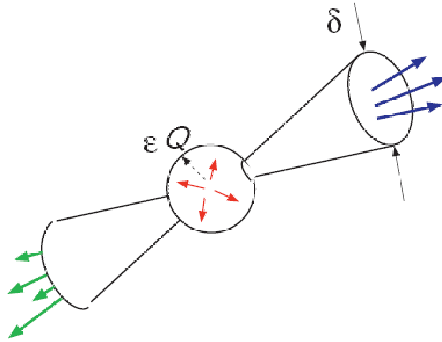
Fig. 17: Dijet final state in $e^- e^+$ annihilation.

cancellation is not complete, and logarithmic enhancement appears. The explicit NLO calculations imply that the isotropic soft gluons give a contribution proportional to $2\ln^2(2\epsilon Q/\mu) - \pi^2/6$, the collinear gluons in the cones with energy higher than the resolution give $-3\ln(Q\delta/\mu) - 2\ln^2(2\epsilon) - 4\ln(Q\delta/\mu)\ln(2\epsilon) + 17/4 - \pi^2/3$, and the virtual corrections contribute $-2\ln^2(Q/\mu) + 3\ln(Q/\mu) - 7/4 + \pi^2/6$. The total NLO corrections indicate that the dijet cross section is infrared finite, but logarithmically enhanced:

$$3\ln\delta + 4\ln\delta\ln(2\epsilon) + \frac{\pi^2}{3} - \frac{5}{2}, \tag{73}$$

where the double logarithm $\ln\delta\ln(2\epsilon)$ is attributed to the overlap of the collinear and soft logarithms.

4.1 Jet in Experiments

To describe the kinematics for jets, we define the pseudorapidity $\eta = \ln[\cot(\theta/2)]$, which is related to the polar angle θ with respect to the beam direction, and the azimuthal angle ϕ. That is, $\theta = 0, 90°$, and $180°$ correspond to $\eta = +\infty, 0$ and $-\infty$, respectively. Comparison of theoretical and experimental descriptions for jet observables is nontrivial. One needs jet algorithms that map experimental measurements with theoretical calculations as close as possible. The infrared safety [61] is an important guideline for setting up a jet algorithm. There are two major classes of jet algorithms in the literature: cone algorithms and sequential algorithms. The former is a geometrical method, which stamps out jets on the η-ϕ plane as with a cookie cutter. The latter combines particle four-momenta one by one following given kinematic criteria.

I take the seeded cone algorithm as an example to explain the operation in the first class of jet algorithms, which aims at finding stable cones via an iterative procedure. Start from a seed particle i, and consider a set of particles j with separations smaller than jet cone of radius R,

$$\Delta R_{ij}^2 \equiv (\eta_i - \eta_j)^2 + (\phi_i - \phi_j)^2 < R^2. \tag{74}$$

Calculate the new cone center J by summing all particle four-momenta in the cone. A stable cone is composed of a set of particles i satisfying $\Delta R_{iJ} < R$. If the cone is stable, the procedure stops. Otherwise, take J as a new seed, and repeat the above procedure.

However, the seeded cone algorithm suffers the problem of infrared divergences. Such a geometrical algorithm does not differentiate infrared gluons from energetic gluons, so final outcomes depend on soft radiation and collinear splitting. This problem can be illustrated by considering a system of two particles 1 and 2, separated by R_{12} with $R < R_{12} < 2R$. Each of particles 1 and 2, taken as a seed, forms a stable jet. One then adds a soft gluon to this system. It is obvious that a virtual soft gluon exchanged between jets 1 and 2 does not change the outcome; namely, a virtual soft gluon contributes to the dijet cross section. On the contrary, adding a real soft seed between jets 1 and 2 will merge the two jets because of $R < R_{12} < 2R$. Therefore, a real soft gluon contributes to the single jet cross section. As

a result, the soft divergences do not cancel between the virtual and real corrections. One may speculate that starting from the hardest particle may avoid the difficulty caused by the soft seed. It turns out that the collinear splitting would change the outcome. Including a more energetic particle into the above system, which is emitted between particles 1 and 2. Taking this central particle as the seed, one constructs a single stable jet formed by the three particles. A self-energy correction to the central particle does not change this final state, and contributes to the single jet cross section. However, the splitting of the central particle may produce two particles, which are less energetic than particles 1 and 2. Then one has to take particle 1 or 2 as the seed, and ends up with two stable jets. That is, the collinear splitting contributes to the dijet cross section, and there is no cancellation between virtual and real corrections. It is concluded that a seeded cone algorithm is not infrared safe.

Next I introduce sequential algorithms by taking the k_T algorithm as an example. For any pair of particles i and j, find the minimum of the following three distances

$$d_{ij} = \min(k_{Ti}^2, k_{Tj}^2)\frac{\Delta R_{ij}^2}{R^2}, \quad d_{iB} = k_{Ti}^2, \quad d_{jB} = k_{Tj}^2, \tag{75}$$

with k_T being is a jet transverse momentum. If the minimum is d_{iB} or d_{jB}, i or j is a jet, and removed from the list of particles. Otherwise, i and j are merged into a new jet. Repeat the above procedure until no particles are left. The other sequential algorithms include the Cambridge/Aachen and anti-k_T ones with the definitions of the distances

$$d_{ij} = \frac{\Delta R_{ij}^2}{R^2}, \quad d_{iB} = 1, \quad d_{jB} = 1,$$

$$d_{ij} = \min(k_{Ti}^{-2}, k_{Tj}^{-2})\frac{\Delta R_{ij}^2}{R^2}, \quad d_{iB} = k_{Ti}^{-2}, \quad d_{jB} = k_{Tj}^{-2}, \tag{76}$$

respectively. The grouping starts from soft (energetic) particles and usually leads to an irregular (round) jet shape in the k_T (anti-k_T) algorithm. Note that a sequential algorithm differentiates infrared gluons from energetic ones: adding a soft real gluon does not modify a cone center, so it does not change the outcome.

4.2 Jets in Theory

As outlined in the Introduction, we intend to establish a theoretical framework for jet study, following the idea of the factorization theorem for the DIS in Sec. 2. At NLO, a jet is produced in DIS, as the gluon emitted by the initial-state or final-state quark is collimated to the final-state quark. The restricted phase space of the final-state quark and the gluon in a small angular separation renders an incomplete cancellation between the virtual and real corrections. Hence, jet production is expected to be enhanced by collinear dynamics. Similarly, the initial-state quark propagator can be eikonalized in this collinear region, such that collinear gluons are detached from the initial-state quark and absorbed into a jet function. To all orders, the collinear gluons are collected by the Wilson link with the path-ordered exponential

$$W = \mathcal{P}\exp\left[-ig\int_0^\infty dz n \cdot A(zn)\right], \tag{77}$$

with an arbitrary vector n. The collinear gluon emitted by the final-state quark can be factorized into the jet function straightforwardly by applying the Fierz transformation. A more sophisticated factorization formula for the jet production in the DIS is then written as a convolution of a hard kernel H with a PDF and a jet function J. H denotes the contribution with the collinear pieces for the initial and final states being subtracted. This factorization formalism is the basis for the application of pQCD to jet physics.

The light-quark and gluon jet functions are defined by [62]

$$J_q(M_J^2, P_T, \nu^2, R, \mu^2) = \frac{(2\pi)^3}{2\sqrt{2}(P_J^0)^2 N_c}\sum_{N_J} Tr\left\{\not{\xi}\langle 0|q(0)W^{(\bar{q})\dagger}|N_J\rangle\langle N_J|W^{(\bar{q})}\bar{q}(0)|0\rangle\right\}$$
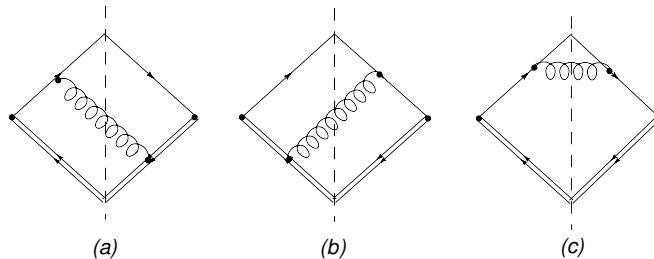
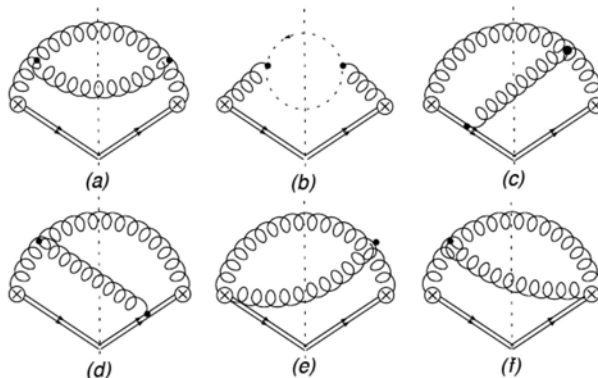**Fig. 18:** Some NLO real corrections to the quark jet function.

Fig. 19: Some NLO real corrections to the gluon jet function, where the dashed line represents a ghost field.

$$\times \delta(M_J^2 - \hat{M}_J^2(N_J, R))\delta^{(2)}(\hat{e} - \hat{e}(N_J))\delta(P_J^0 - \omega(N_J)),$$

$$J_g(M_J^2, P_T, \nu^2, R, \mu^2) = \frac{(2\pi)^3}{2(P_J^0)^3 N_c} \sum_{N_J} \langle 0|\xi_\sigma F^{\sigma\nu}(0)W^{(g)\dagger}|N_J\rangle\langle N_J|W^{(g)}F_\nu^\rho(0)\xi_\rho|0\rangle$$

$$\times \delta(M_J^2 - \hat{M}_J^2(N_J, R))\delta^{(2)}(\hat{e} - \hat{e}(N_J))\delta(P_J^0 - \omega(N_J)), \qquad (78)$$

where $|N_J\rangle$ denotes the final state with N_J particles within the cone of size R centered in the direction of the unit vector $\hat{e}$, $\hat{M}_J(N_J, R)$ ($\omega(N_J)$) is the invariant mass (total energy) of all N_J particles, and μ is the factorization scale. The above jet functions absorb the collinear divergences from all-order radiations associated with the energetic light jet of momentum $P_J^\mu = P_J^0 v^\mu$, in which P_J^0 is the jet energy, and the vector v is given by $v^\mu = (1, \beta, 0, 0)$ with $\beta = \sqrt{1 - (M_J/P_J^0)^2}$. $\xi^\mu = (1, -1, 0, 0)$ is a vector on the light cone. The coefficients in Eq. (78) have been chosen, such that the LO jet functions are equal to $\delta(M_J^2)$ in a perturbative expansion.

Underlying events include everything but hard scattering, such as initial-state radiation, final-state radiation, and multiple parton interaction (MPI). The Wilson lines in Eq. (78) have collected gluons radiated from both initial states and other final states in a scattering process, and collimated to the light-particle jets. Gluon exchanges between the quark fields q (or the gluon fields $F^{\sigma\nu}$ and F_ν^ρ) correspond to the final-state radiations. Both the initial-state and final-state radiations are leading-power effects in the factorization theorem, and have been included in the jet function definition. A chance of involving more partons in hard scattering is low, so the contribution from MPI is regarded as being subleading-power. This contribution should be excluded from data, but it is certainly difficult to achieve in experiments. Nevertheless, it still makes sense to compare predictions for jet observables based on Eq. (78) at the current leading-power accuracy with experimental data. At last, pile-up events must be removed in experiments [63], since they cannot be handled theoretically so far.

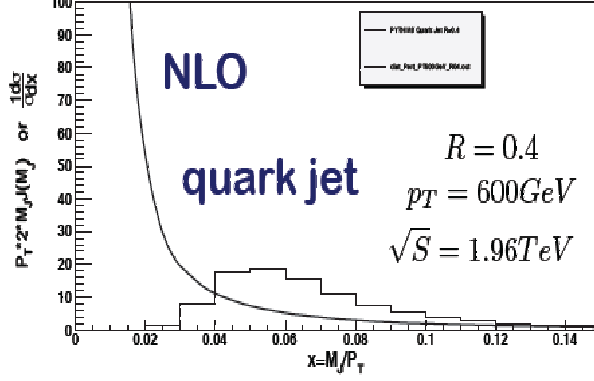The NLO diagrams for the light-quark and gluon jet functions are displayed in Figs. 18 and 19,

Fig. 20: Jet mass distribution at NLO.

respectively. Evaluating the jet functions up to NLO, a divergence is observed at small jet invariant mass M_J as shown in Fig. 20, that implies the nonperturbtive nature of the jet functions. The total NLO corrections in Mellin space indicate the existence of double logarithms, which hint the implementation of the resummation technique. Both the angular and energy resolutions are related to the jet mass: when M_J is not zero, particles in a jet cannot be completely collimated, and the jet must have finite minimal energy. This accounts for the source of the double logarithms. Recall that low p_T spectra of direct photons, dominated by soft and collinear radiations, are treated by the k_T resummation. The jet invariant mass is attributed to soft and collinear radiations, so the mass distribution can also be derived in the resummation formalism.

Varying the Wilson line direction n, we derive the differential equation for the light-quark jet function [64]

$$-\frac{n^2}{v \cdot n}v_\alpha\frac{d}{dn_\alpha}J_q(M_J^2, P_T, \nu^2, R, \mu^2) = 2(K + G) \otimes J_q(M_J^2, P_T, \nu^2, R, \mu^2). \tag{79}$$

The above equation implies that the soft gluons in K are associated with the jet function J, a feature consistent with the anti-k_T algorithm. The solution to Eq. (79) resums the double logarithms in the jet function. One then convolutes the light-quark and gluon jet functions with the constituent cross sections of LO partonic dijet processes at the Tevatron and the PDF CTEQ6L [65]. The resummation predictions for the jet mass distributions at $R = 0.4$ and $R = 0.7$ are compared to the Tevatron CDF data [66] in Fig. 21 [67] with the kinematic cuts $P_T > 400$ GeV and the rapidity interval $0.1 < |Y| < 0.7$. The abbreviation NLL refers to the accuracy of the resummation, and NLO to the accuracy of the initial condition of the jet function solved from Eq. (79). The consistency of the resummation results with the CDF data is satisfactory.

4.3 Jet Substructure

It is known that a top quark produced almost at rest at the Tevatron can be identified by measuring isolated jets from its decay. However, this strategy does not work for identifying a highly-boosted top quark produced at the LHC. It has been observed that an ordinary high-energy QCD jet [68, 69] can have an invariant mass close to the top quark mass. A highly-boosted top quark, producing only a single jet, is then difficult to be distinguished from a QCD jet. This difficulty also appears in the identification of a highly-boosted new-physics resonance decaying into standard-model particles, or Higgs boson decaying into a bottom-quark pair. Hence, additional information needs to be extracted from jet internal structures in order to improve the jet identification at the LHC. The quantity, called planar flow [70], has been proposed for this purpose, which utilizes the geometrical shape of a jet: a QCD jet with large invariant mass mainly involves one-to-two splitting, so it leaves a linear energy deposition in a detector. A top-quark jet,
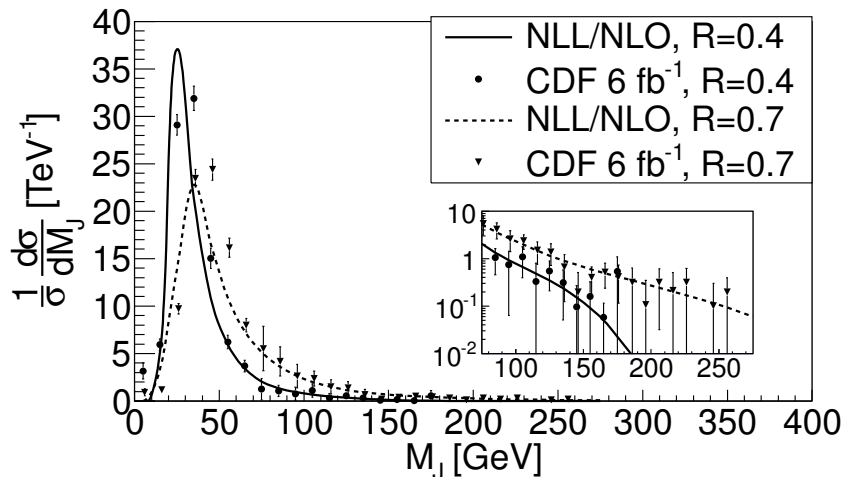
Fig. 21: Comparison of resummation predictions for the jet mass distributions to Tevatron CDF data with the kinematic cuts $P_T > 400$ GeV and $0.1 < |Y| < 0.7$ at $R = 0.4$ and $R = 0.7$. The inset shows the detailed comparison in large jet mass region.

proceeding with a weak decay, mainly involves one-to-three splitting, so it leaves a planar energy deposition. Measuring this additional information, it has been shown with event generators that the top-quark identification can be improved to some extent. Investigations on various observables associated with jet substructures are usually done using event generators. For a review on recent theoretical progress and the latest experimental results in jet substructures, see [71].

Here I focus on a jet substructure, called the energy profile, and explain how to calculate it in the resummation formalism [64]. This quantity describes the energy fraction accumulated in the cone of size r within a jet cone R, i.e., $r < R$. Its explicit definition is given by [72]

$$\Psi(r) = \frac{1}{N_J} \sum_J \frac{\sum_{r_i < r, i \in J} P_{Ti}}{\sum_{r_i < R, i \in J} P_{Ti}}, \tag{80}$$

with the normalization $\Psi(R) = 1$, where P_{Ti} is the transverse momentum carried by particle i in the jet J, and $r_i < r$ ($r_i < R$) means the flow of particle i into the jet cone r (R). Different types of jets are expected to exhibit different energy profiles. For example, a light-quark jet is narrower than a gluon jet; that is, energy is accumulated faster with r in a light-quark jet than in a gluon jet. A heavy-particle jet certainly has a distinct energy profile, which can be used for its identification. The importance of higher-order corrections and their resummation for studying a jet energy profile have been first emphasized in [73]. Another approach based on the soft-collinear effective theory and its application to jet production at an electron-positron collider can be found in Refs. [74–76].

We first define the jet energy functions $J_f^E(M_J^2, P_T, \nu^2, R, r)$ with $f = q(g)$ denoting the light-quark (gluon), which describe the energy accumulation within the cone of size $r < R$. The definition is chosen, such that $J_f^{E(0)} = P_T \delta(M_J^2)$ at LO. The Feynman rules for J_f^E are similar to those for the jet functions J_f at each order of α_s, except that a sum of the step functions $\sum_i k_i^0 \Theta(r - \theta_i)$ is inserted, where k_i^0 (θ_i) is the energy (the angle with respect to the jet axis) of particle i. For example, the jet energy functions J_f^E are expressed, at NLO, as

$$\begin{aligned}
J_q^{E(1)}(M_J^2, P_T, \nu^2, R, r, \mu^2) &= \frac{(2\pi)^3}{2\sqrt{2}(P_J^0)^2 N_c} \sum_{\sigma, \lambda} \int \frac{d^3p}{(2\pi)^3 2p^0} \frac{d^3k}{(2\pi)^3 2k^0} \\
&\times [p^0 \Theta(r - \theta_p) + k^0 \Theta(r - \theta_k)] \\
&\times \mathrm{Tr} \left\{ \not{\xi} \langle 0|q(0) W^{(\bar{q})\dagger}|p, \sigma; k, \lambda\rangle \langle k, \lambda; p, \sigma| W^{(\bar{q})} \bar{q}(0)|0\rangle \right\}
\end{aligned}$$

$$\times \delta(M_J^2 - (p+k)^2)\delta^{(2)}(\hat{e} - \hat{e}_{\mathbf{p+k}})\delta(P_J^0 - p^0 - k^0),$$

$$J_g^{E(1)}(M_J^2, P_T, \nu^2, R, r, \mu^2) = \frac{(2\pi)^3}{2(P_J^0)^3 N_c} \sum_{\sigma,\lambda} \int \frac{d^3p}{(2\pi)^3 2p^0} \frac{d^3k}{(2\pi)^3 2k^0}$$

$$\times [p^0 \Theta(r - \theta_p) + k^0 \Theta(r - \theta_k)]$$

$$\times \langle 0|\xi_\sigma F^{\sigma\nu}(0)W^{(g)\dagger}|p,\sigma;k,\lambda\rangle\langle k,\lambda;p,\sigma|W^{(g)}F_\nu^\rho(0)\xi_\rho|0\rangle$$

$$\times \delta(M_J^2 - (p+k)^2)\delta^{(2)}(\hat{e} - \hat{e}_{\mathbf{p+k}})\delta(P_J^0 - p^0 - k^0), \qquad (81)$$

where the expansion of the Wilson links in α_s is understood. The factorization scale is set to $\mu = P_T$ to remove the associated logarithms, so its dependence will be suppressed below.

The Mellin-transformed jet energy function $\bar{J}_q^E$ obeys a similar differential equation [64]

$$-\frac{n^2}{v \cdot n} v_\alpha \frac{d}{dn_\alpha} \bar{J}_q^E(N = 1, P_T, \nu^2, R, r) = 2(\bar{K} + G)\bar{J}_q^E(N = 1, P_T, \nu^2, R, r), \qquad (82)$$

which can be solved simply. Inserting the solutions to Eq. (82) into Eq. (80), the jet energy profile is derived. Note that a jet energy profile with $N = 1$ is not sensitive to the nonperturbative contribution, so the predictions are free of the nonperturbative parameter dependence, in contrast to the case of the jet invariant mass distribution. It has been found that the light-quark jet has a narrower energy profile than the gluon jet, as exhibited in Fig. 22 for $\sqrt{s} = 7$ TeV and the interval 80 GeV $< P_T <$ 100 GeV of the jet transverse momentum. The broader distribution of the gluon jet results from stronger radiations caused by the larger color factor $C_A = 3$, compared to $C_F = 4/3$ for a light-quark jet.
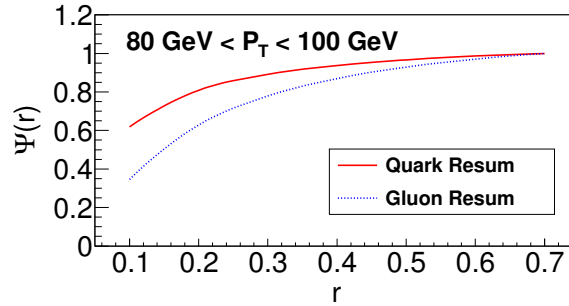

Fig. 22: Resummation predictions for the energy profiles of the light-quark (solid curve) and gluon (dotted curve) jets with $\sqrt{s} = 7$ TeV and 80 GeV $< P_T <$ 100 GeV.
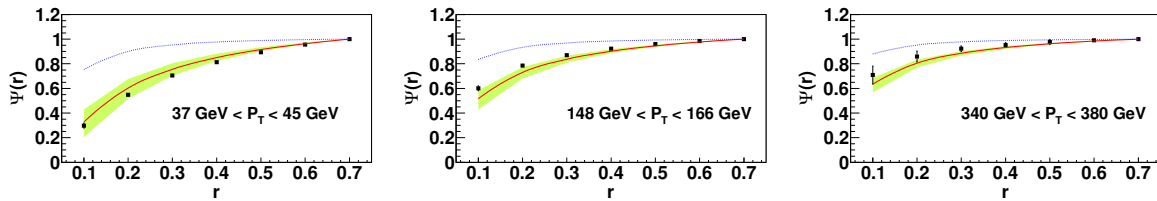

Fig. 23: Comparison of resummation predictions for the jet energy profiles with $R = 0.7$ to Tevatron CDF data in various P_T intervals. The NLO predictions denoted by the dotted curves are also displayed.

One then convolutes the light-quark and gluon jet energy functions with the constituent cross sections of the LO partonic subprocess and CTEQ6L PDFs [65] at certain collider energy. The predictions are directly compared with the Tevatron CDF data [72] as shown in Fig. 23. It is evident that the resummation predictions agree well with the data in all P_T intervals. The NLO predictions derived from $\bar{J}_f^{E(1)}(1, P_T, \nu_{\mathrm{fi}}^2, R, r)$ are also displayed for comparison, which obviously overshoot the data. The resummation predictions for the jet energy profiles are compared with the LHC CMS data at 7 TeV [77]

from the anti-k_T jet algorithm [78] in Fig. 24, which are also consistent with the data in various P_T intervals. Since one can separate the contributions from the light-quark jet and the gluon jet, the comparison with the CDF and CMS data implies that high-energy (low-energy) jets are mainly composed of the light-quark (gluon) jets. Hence, a precise measurement of the jet energy profile as a function of jet transverse momentum can be used to experimentally discriminate the production mechanism of jets in association with other particles, such as electroweak gauge bosons, top quarks and Higgs bosons.
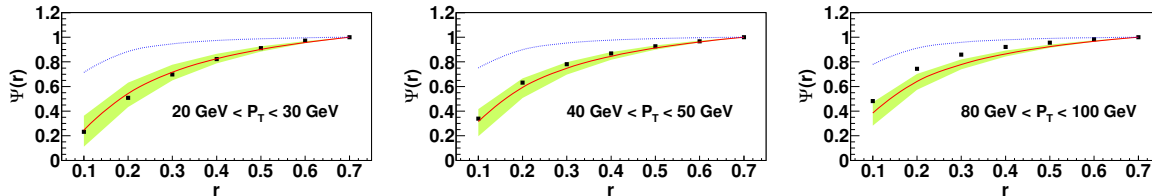

Fig. 24: Resummation predictions for the jet energy profiles with $R = 0.7$ compared to LHC CMS data in various P_T intervals. The NLO predictions denoted by the dotted curves are also displayed.

5   Hadronic heavy-quark decays

Hadronic decays of heavy-quark bound states, such as B, B_s, and Λ_b, are one of the focuses of LHCb physics, whose precision measurement may reveal new physics in the flavor sector. They are difficult to analyze theoretically because of complicated QCD dynamics and multiple characteristic scales they involve: the W boson mass m_W, the b quark mass m_b, and the QCD scale $\Lambda_{\rm QCD}$. The standard procedure is first to integrate out the scale m_W, such that QCD dynamics is organized into an effective weak Hamiltonian [79]. For the $B \to D\pi$ decays, the effective Hamiltonian is written as

$$\mathcal{H}_{\rm eff} = \frac{G_F}{\sqrt{2}} V_{cb}V_{ud}^* \Big[C_1(\mu)O_1(\mu) + C_2(\mu)O_2(\mu) \Big], \tag{83}$$

where G_F is the Fermi coupling constant, $V_{cb}V_{ud}^*$ is the product of the Cabibbo-Kobayashi-Maskawa matrix elements, μ is the renormalization scale, $C_{1,2}$ are the Wilson coefficients, and the four-fermion operators are defined by

$$O_1 = (\bar{d}b)_{V-A}(\bar{c}u)_{V-A} \,, \qquad O_2 = (\bar{c}b)_{V-A}(\bar{d}u)_{V-A}. \tag{84}$$

For exclusive processes, such as hadron form factors, the collinear factorization was developed in [80–83]. The range of a parton momentum fraction x, contrary to that in the inclusive case, is not experimentally controllable, and must be integrated over between 0 and 1. Hence, the end-point region with a small x is not avoidable. If there is no end-point singularity developed in a hard kernel, the collinear factorization works. If such a singularity occurs, indicating the breakdown of the collinear factorization, the k_T factorization should be employed, because the parton transverse momentum k_T is not negligible. To derive $B \to D\pi$ decay amplitudes, one evaluates the hadronic matrix elements $\langle D\pi|O_i(\mu)|B\rangle$. Different theoretical approaches have been developed for this purpose, which include the factorization assumption, the QCD-improved factorization, the perturbative QCD, the soft-collinear effective theory, the light-cone QCD sum rules, and the quark-diagram parametrization. In this section I briefly introduce the basic ideas of the first three approaches [24].

5.1   Factorization Assumption

Intuitively, decay products from a heavy b quark move fast without further interaction between them. This naive picture is supported by the color-transparency argument [84]: the Lorentz contraction renders energetic final states emitted from the weak vertex have small longitudinal color dipoles, which cannot

be resolved by soft gluons. Therefore, the hadronic matrix element $\langle O(\mu) \rangle$ is factorized into a product of two matrix elements of single currents, governed by decay constants and form factors, without soft gluon exchanges between them. This factorization assumption (FA) [14] was first proved in the framework of large energy effective theory [85], and justified in the large N_c limit [86]. For the $B \to D\pi$ decays, the color-allowed (color-suppressed) amplitude, involving the $B \to D$ ($B \to \pi$) transition form factor, is proportional to the Wilson coefficient $a_1 = C_2 + C_1/N_c$ ($a_2 = C_1 + C_2/N_c$).

In spite of its simplicity, the FA encounters three principal difficulties. First, a hadronic matrix element under the FA is independent of the renormalization scale μ, as the vector or axial-vector current is partially conserved. Consequently, the amplitude $C(\mu)\langle O \rangle_{\text{fact}}$ is not truly physical as the scale dependence of the Wilson coefficient does not get compensation from the matrix element. This problem may not be serious for color-allowed modes, because the parameter a_1 is roughly independent of μ. It is then not a surprise that the simple FA gives predictions in relatively good agreement with data of these modes. However, the parameter a_2 depends strongly on the renormalization scale and on the renormalization scheme, because of the similar magnitude and different sign of the $C_1(\mu)$ and $C_2(\mu)/N_c$ terms (calculated in the NDR scheme and for $\Lambda_{\overline{MS}}^{(5)} = 225$ GeV, the Wilson coefficients have the values $C_1(m_B) = -0.185$ and $C_2(m_B) = 1.082$ [79], m_B being the B meson mass). This may be the reason why the FA fails to accommodate data of color-suppressed modes. It also means that a_2 is more sensitive to subleading contributions.

The second difficulty is related to the first one: nonfactorizable effects have been neglected in the FA. This neglect may be justified for color-allowed modes due to the large and roughly μ-independent value of a_1, but not for color-suppressed modes, such as $B \to J/\psi K^{(*)}$. The J/ψ meson emitted from the weak vertex is not energetic, and the color-transparency argument does not apply. To circumvent this difficulty, nonfactorizable contributions were parameterized into the parameters χ_i [87, 88],

$$
\begin{aligned}
a_1^{\text{eff}} &= C_2(\mu) + C_1(\mu)\left[\frac{1}{N_c} + \chi_1(\mu)\right], \\
a_2^{\text{eff}} &= C_1(\mu) + C_2(\mu)\left[\frac{1}{N_c} + \chi_2(\mu)\right].
\end{aligned}
\tag{85}
$$

The μ dependence of the Wilson coefficients is assumed to be exactly compensated by that of $\chi_i(\mu)$ [89]. It is obvious that the introduction of χ_i does not really resolve the scale problem in the FA.

Third, strong phases are essential for predicting CP asymmetries in exclusive B meson decays. These phases, arising from the Bander-Silverman-Soni (BSS) mechanism [90], are ambiguous in the FA: the charm quark loop contributes an imaginary piece proportional to

$$
\int du\, u(1-u)\theta(q^2 u(1-u) - m_c^2),
\tag{86}
$$

where q^2 is the invariant mass of the gluon attaching to the charm loop. Since q^2 is not precisely defined in the FA, one cannot obtain definite information of strong phases from Eq. (86). Moreover, it is legitimate to question whether the BSS mechanism is an important source of strong phases in B meson decays. Viewing the above difficulties, the FA is not a complete model, and it is necessary to go beyond the FA by developing reliable and systematic theoretical approaches.

5.2 QCD-improved Factorization

The color-transparency argument allows the addition of hard gluons between the energetic mesons emitted from the weak vertex and the B meson transition form factors. These hard gluon exchanges lead to higher-order corrections in the coupling constant α_s to the FA. By means of Feynman diagrams, they appear as the vertex corrections in the first two rows of Fig. 25 [15]. It has been shown that soft divergences cancel among them, when computed in the collinear factorization theorem. These $O(\alpha_s)$
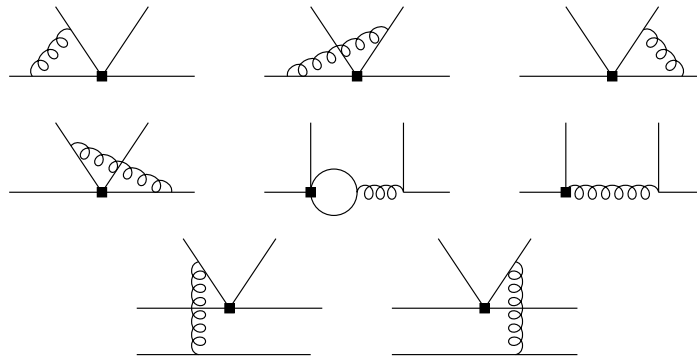
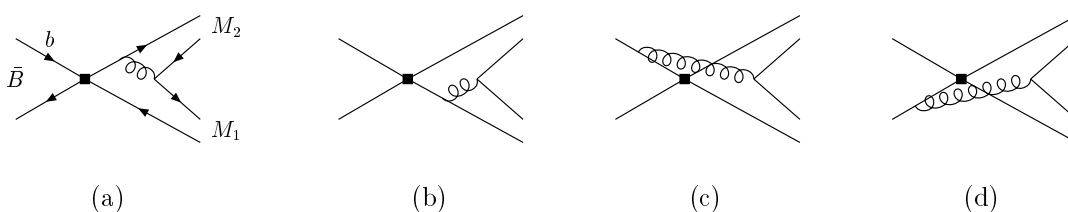**Fig. 25:** $O(\alpha_s)$ corrections to the FA in the QCDF approach.

Fig. 26: Annihilation contributions.

corrections weaken the μ dependence in the Wilson coefficients, and generate strong phases. Besides, hard gluons can also be added to form the spectator diagrams in the last row of Fig. 25. Feynman rules of these two diagrams differ by a minus sign in the soft region resulting from the involved quark and anti-quark propagators. Including the above nonfactorizable corrections to the FA leads to the QCD-improved factorization (QCDF) approach [15]. The gluon invariant mass q^2 in the BSS mechanism can be unambiguously defined and related to parton momentum fractions in QCDF. Hence, the theoretical difficulties in the FA are resolved. This is a breakthrough towards a rigorous framework for two-body hadronic B meson decays in the heavy quark limit.

Corrections in higher powers of $1/m_b$ to the FA can also be included into QCDF, such as those from the annihilation topology in Fig. 26, and from twist-3 contributions to the spectator amplitudes. However, it has been found that endpoint singularities exist in these high-power contributions, which arise from the divergent integral $\int_0^1 dx/x$, x being a momentum fraction. These singularities have the same origin as those in the collinear collinear factorization formulas for B meson transition form factors [91]. Because of the endpoint singularities, the annihilation and twist-3 spectator contributions must be parameterized as [15]

$$\ln \frac{m_B}{\Lambda_h} \left(1 + \rho_A e^{i\delta_A} \right) \ , \quad \ln \frac{m_B}{\Lambda_h} \left(1 + \rho_H e^{i\delta_H} \right) \ , \tag{87}$$

respectively, with the hadronic scale Λ_h. A QCDF formula then contains the arbitrary parameters $\rho_{A,H}$ and $\delta_{A,H}$. Setting these parameters to zero, one obtains predictions in the "default" scenario, and the variation of the arbitrary parameters gives theoretical uncertainties. If tuning these parameters to fit data, one obtains results in the scenarios "S", "S2",... [92].
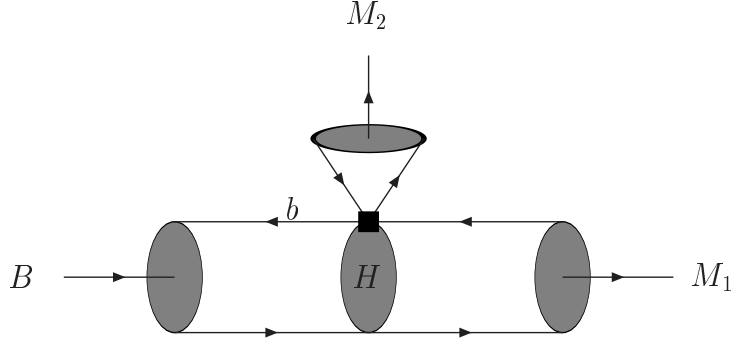
M_2

b

$B \longrightarrow$

H

M_1

Fig. 27: Perturbative QCD factorization.

5.3 Perturbative QCD

The endpoint singularities signal the breakdown of the collinear factorization for two-body hadronic B meson decays. Motivated by the removal of these singularities, the perturbative QCD (PQCD) approach based on the k_T factorization theorem was developed [16–19]. A parton transverse momentum k_T can be generated by gluon radiations, before hard scattering occurs. The endpoint singularities from the small x region simply indicate that k_T is not negligible. Taking into account k_T, a particle propagator does not diverge as $x \to 0$. The B meson transition form factors, and the spectator and annihilation contributions are then all calculable in the framework of the k_T factorization theorem. It has been shown that a $B \to M_1 M_2$ decay amplitude is factorized into the convolution of the six-quark hard kernel, the jet function and the Sudakov factor with the bound-state wave functions as shown in Fig. 27,

$$A(B \to M_1 M_2) = \phi_B \otimes H \otimes J \otimes S \otimes \phi_{M_1} \otimes \phi_{M_2}. \tag{88}$$

The jet function J comes from the threshold resummation, which exhibits suppression in the small x region [93]. The Sudakov factor S comes from the k_T resummation, which exhibits suppression in the small k_T region [39, 40]. These resummation effects guarantee the removal of the endpoint singularities. J (S), organizing double logarithms in the hard kernel (meson wave functions), is hidden in H (the three meson states) in Fig. 27. The arbitrary parameters introduced in QCDF are not necessary, and PQCD involves only universal and controllable inputs.

The theoretical difficulties in the FA are also resolved in PQCD but in a different manner. The FA limit of the PQCD approach at large m_b, which is not as obvious as in QCDF, has been examined [93]. It was found that the factorizable emission amplitude decreases like $m_b^{-3/2}$, if the B meson decay constant f_B scales like $f_B \propto m_b^{-1/2}$. This power-law behavior is consistent with that obtained in [15, 94]. The higher-order corrections to the FA have been included in PQCD, which moderate the dependence on the renormalization scale μ. The ratio of the spectator contribution over the factorizable emission contribution decreases with m_b in PQCD, showing a behavior close to that in QCDF. The gluon invariant mass q^2 in the BSS mechanism is unambiguously defined and related to parton momentum fractions. The penguin annihilation amplitude is almost imaginary in PQCD [18], whose mechanism is similar to the BSS one [90]: in the annihilation topology, the loop is formed by the internal particles in the LO hard kernel and by infinitely many Sudakov gluons exchanged between two partons in a light meson. A sizable strong phase is generated, when the internal particles go on mass shell. In terms of the principal-value prescription for the internal particle propagator, the strong phase is given by [18]

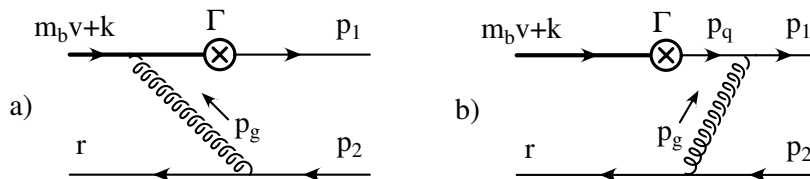$$\frac{1}{xm_B^2 - k_T^2 + i\epsilon} = \frac{P}{xm_B^2 - k_T^2} - i\pi\delta(xm_B^2 - k_T^2). \tag{89}$$

127

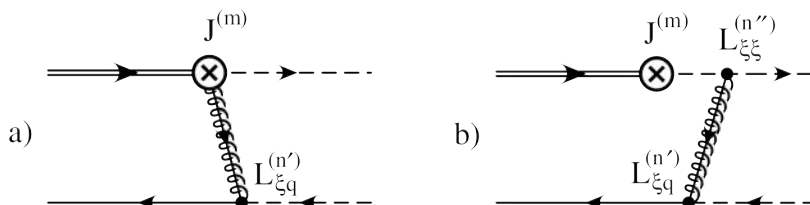**Fig. 28:** Diagrams for the $B \to \pi$ form factor in QCD.

Fig. 29: Diagrams for the $B \to \pi$ form factor in SCET$_\mathrm{I}$.

5.4 Soft-Collinear Effective Theory

The soft-collinear effective theory (SCET) based on the collinear factorization is formulated in the framework of OPE [20–23]. The matching at different scales involved in B meson decays has been carefully handled in SCET. Take the simple $B \to \pi$ transition form factor in Fig. 28 as an example. The soft spectator in the B meson carries the momentum $r \sim O(\Lambda_{\mathrm{QCD}})$, because it is dominated by soft dynamics. If the spectator in the energetic pion carries the momentum $p_2 \sim O(m_b)$, the virtual gluon in Fig. 28 is off-shell by $p_g^2 = (p_2 - r)^2 = -2p_2 \cdot r \sim O(m_b \Lambda_{\mathrm{QCD}})$. Then the virtual quark in Figs. 28(a) is off-shell by $(m_b v + k + p_g)^2 - m_b^2 \sim O(m_b^2)$, where v is the b quark velocity and $k \sim O(\Lambda_{\mathrm{QCD}})$ denotes the Fermi motion of the b quark. Hence, B meson decays contain three scales below m_W: m_b, $\sqrt{m_b \Lambda_{\mathrm{QCD}}}$, and Λ_{QCD}.

The separate matching at the two scales m_b and $\sqrt{m_b \Lambda_{\mathrm{QCD}}}$ is briefly explained below [95]. The first step is to integrate out the lines off-shell by m_b^2 in QCD, and the resultant effective theory is called SCET$_\mathrm{I}$. One then derives the zeroth-order effective current $J^{(0)}$ from the $b \to u$ weak vertex, and the first-order effective current $J^{(1)}$ by shrinking the virtual b quark line in Fig. 28(a). The next step is to integrate out the lines off-shell by $m_b \Lambda_{\mathrm{QCD}}$ in SCET$_\mathrm{I}$, arriving at SCET$_\mathrm{II}$. The relevant diagrams to start with are displayed in Fig. 29. Shrinking all the lines off-shell by $m_b \Lambda_{\mathrm{QCD}}$, one derives the corresponding Wilson coefficients, i.e., the jet functions, and the effective four-fermion operators. Sandwiching these four-fermion operators by the initial B meson state and the final pion state leads to the B meson and pion distribution amplitudes. The $B \to \pi$ transition form factor is then factorized as depicted in Fig. 30. The factorization of two-body hadronic B meson decays is constructed in a similar way, and the result is also shown in Fig. 30.

At leading power in $1/m_b$, there is no large source of strong phases in SCET (the annihilation contribution is parametrically power-suppressed). To acquire strong phases, it has been argued that $c\bar{c}$ (charming) penguins could give long-distance effects at leading power [96]. This contribution is nonperturbative, so it must be parameterized as an arbitrary amplitude $A^{c\bar{c}}$. Including the charming penguin, SCET has been applied as an QCD-improved parametrization, and $A^{c\bar{c}}$ is determined together with other hadronic inputs from data. It should be mentioned that the long-distance charming-penguin contribution is power-suppressed according to QCDF, PQCD and light-cone sum rules [97].
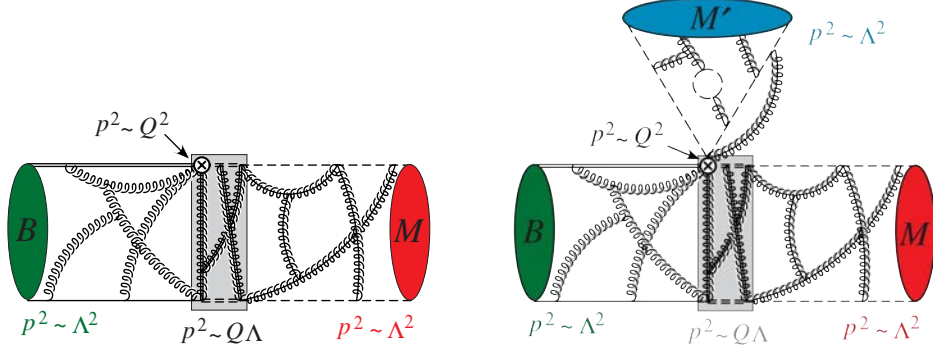
Fig. 30: Factorization of the $B \to \pi$ form factor and of the $B \to M_1 M_2$ decay in SCET.

5.5 Puzzles in B Physics

Before concluding, I review the long-standing puzzles in hadronic two-body B meson decays, which have not yet been fully resolved so far. According to a naive estimate of the color-suppressed tree amplitude, the hierarchy of the branching ratios $B(B^0 \to \pi^0\pi^0) \sim O(\lambda^2)B(B^0 \to \pi^\mp\pi^\pm)$ with the CKM parameter $\lambda \approx 0.2$ is expected. However, the data [98]

$$
\begin{aligned}
B(B^0 \to \pi^\mp\pi^\pm) &= (5.10 \pm 0.19) \times 10^{-6} \,, \\
B(B^0 \to \pi^0\pi^0) &= (1.91^{+0.22}_{-0.23}) \times 10^{-6} \,,
\end{aligned}
\tag{90}
$$

imply $B(B^0 \to \pi^0\pi^0) \sim O(\lambda)B(B^0 \to \pi^\mp\pi^\pm)$, giving rise to the $B \to \pi\pi$ puzzle. As observed in [99], the NLO corrections, despite of increasing the color-suppressed tree amplitude significantly, are not enough to enhance the $B^0 \to \pi^0\pi^0$ branching ratio to the measured value. A much larger color-suppressed tree amplitude, about the same order as the color-allowed tree amplitude, must be obtained in order to resolve the puzzle [100, 101]. To make sure that the above NLO effects are reasonable, the PQCD formalism has been applied to the $B \to \rho\rho$ decays [99], which also receive the color-suppressed tree contribution. It was observed that the NLO PQCD predictions are in agreement with the data $B(B^0 \to \rho^0\rho^0) = (0.73^{+0.27}_{-0.28}) \times 10^{-6}$ [98]. One concludes that it is unlikely to accommodate the measured $B^0 \to \pi^0\pi^0$ and $\rho^0\rho^0$ branching ratios simultaneously in PQCD, and that the $B \to \pi\pi$ puzzle remains.

It has been claimed that the $B \to \pi\pi$ puzzle has been resolved in the QCDF approach [15] with an input from SCET [102–104]: the inclusion of the NLO jet function, the hard coefficient of SCET$_{\rm II}$, into the QCDF formula for the color-suppressed tree amplitude gives sufficient enhancement of the $B^0 \to \pi^0\pi^0$ branching ratio, if adopting the parameter scenario "S4" [105]. It is necessary to investigate whether the proposed new mechanism deteriorates the consistency of theoretical results with other data. The formalism in [102] has been extended to the $B \to \rho\rho$ decays as a check [99]. It was found that the NLO jet function overshoots the observed $B^0 \to \rho^0\rho^0$ branching ratio very much as adopting "S4". That is, it is also unlikely to accommodate the $B \to \pi\pi$ and $\rho\rho$ data simultaneously in QCDF.

Table 1: Polarization fractions in the penguin-dominated $B \to VV$ decays.

Mode	BABAR	Belle
ϕK^{*+}	$0.49 \pm 0.05 \pm 0.03$	$0.52 \pm 0.08 \pm 0.03$
$K^{*+}\rho^0$	$0.78 \pm 0.12 \pm 0.03$	
$K^{*0}\rho^+$	$0.52 \pm 0.10 \pm 0.04$	$0.43 \pm 0.11^{+0.05}_{-0.02}$
$K^{*+}K^{*0}$	$0.75^{+0.16}_{-0.26} \pm 0.03$	

For penguin-dominated $B \to VV$ decays, such as those listed in Table 1 [98], the polarization fractions deviate from the naive counting rules based on kinematics [106]. This is the so-called the $B \to \phi K^*$ puzzle. Many attempts to resolve the $B \to \phi K^*$ polarizations have been made [107], which include new physics [108–112], the annihilation contribution [113, 114] in the QCDF approach, the charming penguin in SCET [115], the rescattering effect [116–118], and the $b \to sg$ (the magnetic penguin) [119] and $b \to s\gamma$ [120] transitions. The annihilation contribution from the scalar penguin operators improves the consistency with the data, because it is of the same order for all the three final helicity states, and could enhance the transverse polarization fractions [106]. However, the PQCD analysis of the scalar penguin annihilation amplitudes indicates that the $B \to \phi K^*$ puzzle cannot be resolved completely [107]. A reduction of the $B \to K^*$ form factor A_0, which is associated with the longitudinal polarization, further helps accommodating the data [121].

The penguin-dominated $B \to K^*\rho$ decays are expected to exhibit similar polarization fractions. This is the reason why the longitudinal polarization fraction in the $B^+ \to K^{*0}\rho^+$ decay, which contains only the penguin contribution, is close to $f_L(\phi K^*) \sim 0.5$ as listed in Table 1. Another mode $B^+ \to K^{*+}\rho^0$, nevertheless, exhibits a large longitudinal polarization fraction around 0.8. This mode involves tree amplitudes, which are subdominant, and should not cause a significant deviation from $f_L \sim 0.5$. Though the data of $f_L(K^{*0}\rho^+)$ from BABAR still suffer a large error, the different longitudinal polarization fractions, $f_L(K^{*+}\rho^0) \neq f_L(K^{*0}\rho^+)$, call for a deeper understanding. The $B^+ \to K^{*+}K^{*0}$ decay shows a longitudinal polarization fraction smaller than unity, but larger than 0.5. A more thorough study of the $B \to K^*K^*$ decays can help discriminating the various resolutions for the $B \to \phi K^*$ puzzle [121, 122].

The $B^0 \to K^\pm\pi^\mp$ decays depend on the tree amplitude T and the QCD penguin amplitude P. The data of the direct CP asymmetry $A_{CP}(B^0 \to K^\pm\pi^\mp) \approx -10\%$ then imply a sizable relative strong phase between T and P, which verifies the LO PQCD prediction made years ago [18]: the scalar penguin annihilation provides an important source of strong phases. The PQCD predictions for significant penguin annihilation have been confirmed by the recent measurement of the pure annihilation mode, $B(B_s \to \pi^+\pi^-) = (0.73 \pm 0.14) \times 10^{-6}$, which is consistent with 0.57×10^{-6} obtained in the LO PQCD approach [123]. The $B^\pm \to K^\pm\pi^0$ decays contain the additional color-suppressed tree amplitude C and electroweak penguin amplitude P_{ew}. Since both C and P_{ew} are subdominant, the approximate equality for the direct CP asymmetries $A_{CP}(B^\pm \to K^\pm\pi^0) \approx A_{CP}(B^0 \to K^\pm\pi^\mp)$ is expected. However, this naive expectation is in conflict with the data [98],

$$
\begin{aligned}
A_{CP}(B^0 \to K^\pm\pi^\mp) &= -0.086 \pm 0.007 \\
A_{CP}(B^\pm \to K^\pm\pi^0) &= 0.040 \pm 0.021,
\end{aligned}
\tag{91}
$$

making the $B \to K\pi$ puzzle.

While LO PQCD gives a negligible C [18, 19], it is possible that this supposedly tiny amplitude receives a significant subleading correction. Note that the small C is attributed to the accidental cancellation between the Wilson coefficients C_1 and C_2/N_c at the scale of m_b. In [124] the important NLO contributions to the $B \to K\pi$ decays from the vertex corrections, the quark loops, and the magnetic penguins were calculated. It was observed that the vertex corrections increase C by a factor of 3, and induce a large phase about -80° relative to T. The large and imaginary C renders the total tree amplitude $T + C$ more or less parallel to the total penguin amplitude $P + P_{ew}$ in the $B^\pm \to K^\pm\pi^0$ decays, leading to nearly vanishing $A_{CP}(B^\pm \to K^\pm\pi^0) = (-1^{+3}_{-6})\%$ at NLO (it is about -8% at LO). One concludes that the $B \to K\pi$ puzzle has been alleviated, but not yet gone away completely. Whether new physics effects [125, 126] are needed will become clear when the data get precise. More detailed discussion on this subject can be found in [127].

6 Summary

Despite of nonperturbative nature of QCD, theoretical frameworks with predictive power can be developed. They are based on the factorization theorems, in which nonperturbative dynamics is absorbed into PDFs, and the remaining infrared finite contributions go to hard kernels. A PDF is universal (process-independent) and can be extracted from data, while a hard kernel is calculable in perturbation theory. Both the collinear and k_T factorization theorems are the fundamental tools of pQCD. The collinear factorization theorem is a simpler version, and has been intensively studied and widely applied. The k_T factorization theorem is more complicated, and many of its aspects have not been completely explored.

Sophisticated evolution equations and resummation techniques have been developed in pQCD, which enhance predictive power, and increase theoretical precision. All the known single- and double-logarithm summations, including their unifications, have been explained in the CSS resummation formalism. The point is the treatment of real gluon emissions under different kinematic orderings, and the resultant logarithmic summations are summarized in Table 2. The k_T and threshold resummations, and the DGLAP and BFKL equations have been applied to various QCD processes.

Table 2: Single- and double-logarithmic summations under different kinematic orderings.

	small x	intermediate x	large x
rapidity ordering	BFKL equation	k_T resummation	
k_T ordering		DGLAP equation	threshold resummation
angular ordering	CCFM	equation; joint	resummation

Experimental and theoretical studies of jet physics have been reviewed. Especially, it was pointed out that jet substructures could be calculated in pQCD: starting with the jet function definition, applying the factorization theorem and the resummation technique, one can predict observables, which are consistent with data. Because fixed-order calculations are not reliable at small jet invariant mass, and event generators have ambiguities, pQCD provides an alternative approach, that resolves the above difficulties. The pQCD formalism will improve the jet identification and new particle search at the LHC.

We have been able to go beyond the factorization assumption fr hadronic two-body heavy-quark decays by including QCD corrections. Different approaches have been discussed and commented: in QCDF the high-power corrections must be parameterized due to the existence of the endpoint singularities. There are no endpoint singularities in PQCD, which is based on the k_T factorization theorem, and in SCET, which employs the zero-bin subtraction [128]. A major difference arises from the treatment of the annihilation contribution, which is parameterized in QCDF and neglected in SCET, but is the main source of strong phases in PQCD.

Many subtle subjects on pQCD deserve more exploration, including the legitimate definition of TMDs, the gauge invariance of the k_T factorization, resummations of other types of logarithms, such as rapidity logarithms, non-global logarithms, and etc., jet substructures of boosted heavy particles, and the long-standing puzzles in B physics. pQCD remains as one of the most challenging research fields in high-energy physics.

Acknowledgment

References

[1] G. Sterman, arXiv:hep-ph/9606312.

[2] J.C. Collins and G. Sterman, Nucl. Phys. **B 185**, 172 (1981); J.C. Collins and D.E. Soper, Nucl. Phys. **B194**, 445 (1982).

[3] V.N. Gribov and L.N. Lipatov, Sov. J. Nucl. Phys. **15**, 438 (1972); G. Altarelli and G. Parisi, Nucl. Phys. **B126**, 298 (1977); Yu.L. Dokshitzer, Sov. Phys. JETP **46**, 641 (1977).

[4] E.A. Kuraev, L.N. Lipatov and V.S. Fadin, Sov. Phys. JETP **45**, 199 (1977); Ya.Ya. Balitsky and L.N. Lipatov, Sov. J. Nucl. Phys. **28**, 822 (1978); L.N. Lipatov, Sov. Phys. JETP **63**, 904 (1986).

[5] G. Sterman, Phys. Lett. B **179**, 281 (1986); Nucl. Phys. **B281**, 310 (1987).

[6] S. Catani and L. Trentadue, Nucl. Phys. **B327**, 323 (1989); Nucl. Phys. **B353**, 183 (1991).

[7] G.P. Korchemsky and G. Marchesini, Nucl. Phys. **B406**, 225 (1993); Phys. Lett. B **313**, 433 (1993).

[8] J.C. Collins and D.E. Soper, Nucl. Phys. **B193**, 381 (1981).

[9] J.C. Collins, D.E. Soper, and G. Sterman, Nucl. Phys. **B250**, 199 1985.

[10] M. Ciafaloni, Nucl. Phys. **B296**, 49 (1988); S. Catani, F. Fiorani, and G. Marchesini, Phys. Lett. B **234**, 339 (1990); Nucl. Phys. **B336**, 18 (1990); G. Marchesini, Nucl. Phys. **B445**, 49 (1995).

[11] H.-n. Li, Phys. Lett. B**454**, 328 (1999).

[12] E. Laenen, G. Sterman, and W. Vogelsang, Phys. Rev. Lett. **84**, 4296 (2000); Phys. Rev. D **63**, 114018 (2001).

[13] J. Shelton, arXiv:1302.0260 [hep-ph].

[14] M. Bauer, B. Stech, M. Wirbel, Z. Phys. C **29**, 637 (1985); *ibid.* **34**, 103 (1987).

[15] M. Beneke, G. Buchalla, M. Neubert, and C.T. Sachrajda, Phys. Rev. Lett. **83**, 1914 (1999); Nucl. Phys. **B591**, 313 (2000); Nucl. Phys. **B606**, 245 (2001).

[16] H-n. Li and H.L. Yu, Phys. Rev. Lett. **74**, 4388 (1995); Phys. Lett. B **353**, 301 (1995); Phys. Rev. D **53**, 2480 (1996).

[17] C.H. Chang and H-n. Li, Phys. Rev. D **55**, 5577 (1997).

[18] Y.Y. Keum, H-n. Li, and A.I. Sanda, Phys Lett. B **504**, 6 (2001); Phys. Rev. D **63**, 054008 (2001).

[19] C.D. Lü, K. Ukai, and M.Z. Yang, Phys. Rev. D **63**, 074009 (2001).

[20] C.W. Bauer, S. Fleming, and M. Luke, Phys. Rev. D **63**, 014006 (2001).

[21] C.W. Bauer, S. Fleming, D. Pirjol, and I.W. Stewart, Phys. Rev. D **63**, 114020 (2001).

[22] C.W. Bauer and I.W. Stewart, Phys. Lett. B **516**, 134 (2001).

[23] C.W. Bauer, D. Pirjol and I.W. Stewart, Phys. Rev. D **65**, 054022 (2002).

[24] H.-n. Li, Prog. Part. Nucl. Phys. **51**, 85 (2003).

[25] G. Sterman, *An Introduction to Quantum Field Theory*, Cambridge, 1993.

[26] T. Kinoshta, J. Math. Phys **3**, 650 (1962); T.D. Lee and M. Nauenberg, Phys. Rev. **133**, B1549 (1964).

[27] H.-L. Lai, et al., Phys. Rev. D **82**, 074024 (2010)..

[28] Nadolsky et al., arXiv:1206.3321 [hep-ph].

[29] S. Catani, M. Ciafaloni and F. Hautmann, Phys. Lett. B **242**, 97 (1990); Nucl. Phys. **B366**, 135 (1991).

[30] J.C. Collins and R.K. Ellis, Nucl. Phys. **B360**, 3 (1991).

[31] E.M. Levin, M.G. Ryskin, Yu.M. Shabelskii, and A.G. Shuvaev, Sov. J. Nucl. Phys. **53**, 657 (1991).

[32] X. Ji, and F. Yuan, Phys. Lett. B **543**, 66 (2002); A.V. Belitsky, X. Ji, and F. Yuan, Nucl. Phys. **B656**, 165 (2003).

[33] I.O. Cherednikov and N.G. Stefanis, Nucl. Phys. **B802**, 146 (2008).

[34] H.-n. Li, arXiv:hep-ph/9803202.

[35] J.C. Collins, Acta. Phys. Polon. B **34**, 3103 (2003).

[36] H.-n. Li and S. Mishima, Phys. Lett. B **674**, 182 (2009).

[37] G.P. Korchemsky and G. Sterman, Phys. Lett. B **340**, 96 (1994).

[38] H.-n. Li, Phys. Lett. B369, 137 (1996); Phys. Rev. D **55**, 105 (1997).

[39] J. Botts and G. Sterman, Nucl. Phys. **B325**, 62 (1989).

[40] H.-n. Li and G. Sterman, Nucl. Phys. **B381**, 129 (1992); H.-n. Li, Phys. Rev. D **48**, 4243 (1993).

[41] C. Corianó and H.-n. Li, Phys. Lett. B309, 409 (1993); Nucl. Phys. **B434**, 535 (1995).

[42] H.-n. Li and H.L. Yu, Phys. Rev. Lett. 74, 4388 (1995); Phys. Lett. B353, 301 (1995); H.-n. Li, Phys. Lett. B348, 597 (1995).

[43] H.-n. Li, Phys. Rev. D52, 3958 (1995); C.Y. Wu, T.W. Yeh and H.-n. Li, Phys. Rev. D **53**, 4982 (1996).

[44] J.C. Collins, Adv. Ser. Direct. High Energy Phys. **5**, 573 (1989).

[45] J. Kodaira and L. Trentadue, Phys. Lett. B **112**, 66 (1982).

[46] H.L. Lai and H.-n. Li, Phys. Rev. D **58**, 114020 (1998).

[47] H.L. Lai *et al.*, Phys. Rev. D **55**, 1280 (1997).

[48] T. Becher, C. Lorentzen, and M.D. Schwartz, Phys. Rev. D **86**, 054026 (2012).

[49] H-n. Li, Chin. J. Phys. **37**, 8 (1999); Phys. Lett. B **405**, 347 (1997).

[50] J. Kwieciński, A.D. Martin, and P.J. Sutton, Phys. Rev. D **53**, 6094 (1996).

[51] M. Froissart, Phys. Rev. **123**, 1053 (1961).

[52] V.S. Fadin and L.N. Lipatov, Phys. Lett. B **429**, 127 (1998); G. Camici and M. Ciafaloni, Phys. Lett. B **430**, 349 (1998).

[53] R.S. Thorne, Phys. Rev. D **60**, 054031 (1999).

[54] M. Beneke, P. Falgari, S. Klein, and C. Schwinn, Nucl. Phys. **B855**, 695 (2012).

[55] ATLAS Collaboration, Conference note atlas-conf-2011-121, 2011. https://atlas.web.cern.ch/Atlas/GROUPS/PHYSICS/CONFNOTES/ATLAS-CONF-2011-121/ATLAS-CO.

[56] R. Rajkhowa and J.K. Sarma, arXiv:1209.4350 [hep-ph].

[57] A.D. Martin, R.G. Roberts, W.J. Stirling, and R.S. Thorne, Eur. Phys. J. C **23**, 73 (2002).

[58] M. Devee, R. Baishya, and J.K. Sarma, Eur. Phys. J. C **72**, 2036 (2012).

[59] M. Arneodo et al., Nucl. Phys. **B483**, 3 (1997).

[60] G. Bozzi, B. Fuks, and M. Klasen, Nucl. Phys. **B794**, 46 (2008).

[61] G. Sterman and S. Weinberg, Phys. Rev. Lett. **39**, 1436 (1977).

[62] L.G. Almeida et al., Phys. Rev. D **79**, 074012 (2009).

[63] G. Soyez, G.P. Salam, J. Kim, S. Dutta, and M. Cacciari, arXiv:1211.2811 [hep-ph].

[64] H.-n. Li, Z. Li, Zhao, and C.-P. Yuan, Phys. Rev. Lett. **107**, 152001 (2011).

[65] J. Pumplin et al., JHEP **07**, 012 (2002).

[66] T. Aaltonen et al. (CDF Collaboration), Phys. Rev. D **85**, 091101 (2012).

[67] H.-n. Li, Z. Li, and C.P. Yuan, arXiv:1206.1344 [hep-ph].

[68] W. Skiba and D. Tucker-Smith, Phys. Rev. D **75**, 115010 (2007).

[69] B. Holdom, JHEP **08**, 069 (2007).

[70] L.G. Almeida et al., Phys. Rev. D **79**, 074017 (2009).

[71] A. Altheimer et al., J. Phys. G **39**, 063001 (2012).

[72] D.E. Acosta et al. (CDF Collaboration), Phys. Rev. D **71**, 112002 (2005).

[73] M.H. Seymour, Nucl.Phys. **B513**, 269 (1998).

[74] S.D. Ellis et al., JHEP **11**, 101 (2010).

[75] R. Kelley, M.D. Schwartz, and H.X. Zhu, arXiv: 1102.0561 [hep-ph].

[76] R. Kelley, M.D. Schwartz, R.M. Schabinger, and H.X. Zhu, Phys. Rev. D **86**, 054017 (2012).

[77] CMS Collaboration, Report CMS–PAS–QCD–10–014 (2010).

[78] M. Cacciari, G.P. Salam, and G. Soyez, JHEP **04**, 063 (2008).

[79] G. Buchalla, A. J. Buras, and M. E. Lautenbacher, Review of Modern Physics, **68**, 1125 (1996).

[80] G.P. Lepage and S.J. Brodsky, Phys. Lett. B **87**, 359 (1979); Phys. Rev. D **22**, 2157 (1980).

[81] A.V. Efremov and A.V. Radyushkin, Phys. Lett. B **94**, 245 (1980).

[82] V.L. Chernyak, A.R. Zhitnitsky, and V.G. Serbo, JETP Lett. **26**, 594 (1977).

[83] V.L. Chernyak and A.R. Zhitnitsky, Sov. J. Nucl. Phys. **31**, 544 (1980); Phys. Rep. **112**, 173 (1984).

[84] J.D. Bjorken, Nucl. Phys. Proc. Suppl. **11**, 325 (1989).

[85] M. Dugan and B. Grinstein, Phys. Lett. B **255**, 583 (1991).

[86] A.J. Buras and J.M. Gérard, Nucl. Phys. **B264**, 371 (1986); A.J. Buras, J.M. Gérard, and R. Rückl, Nucl. Phys. **B268**, 16 (1986).

[87] H.Y. Cheng, Phys. Lett. B **335**, 428 (1994); Z. Phys. C **69**, 647 (1996).

[88] J. Soares, Phys. Rev. D **51**, 3518 (1995); A.N. Kamal and A.B. Santra, Z. Phys. C **72**, 91 (1996); A.N. Kamal, A.B. Santra, and R.C. Verma, Phys. Rev. D **53**, 2506 (1996).

[89] M. Neubert, V. Rieckert, B. Stech, and Q.P. Xu, in *Heavy Flavours*, ed. A.J. Buras and M. Lindner (World Scientific, Singapore, 1992); M. Neubert and B. Stech, in *Heavy Flavours II*, ed. A.J. Buras and M. Lindner (World Scientific, Singapore, 1998), hep-ph/9705292.

[90] M. Bander, D. Silverman, and A. Soni, Phys. Rev. Lett. **43**, 242 (1979).

[91] A.P. Szczepaniak, E.M. Henley, and S.J. Brodsky, Phys. Lett. B **243**, 287 (1990).

[92] M. Beneke and M. Neubert Nucl. Phys. **B675**, 333 (2003).

[93] H.-n. Li, Phys. Rev. D **66**, 094010 (2002); H.-n. Li and K. Ukai, Phys. Lett. B **555**, 197 (2003).

[94] V.L. Chernyak and I.R. Zhitnitsky, Nucl. Phys. **B345**, 137 (1990).

[95] C.W. Bauer, D. Pirjol, and I.W. Stewart Phys. Rev. D **67**, 071502 (2003).

[96] C.W. Bauer, D. Pirjol, I.Z. Rothstein, and I.W. Stewart, Phys. Rev. D **70**, 054015 (2004).

[97] A. Khodjamirian, Th. Mannel, and B. Melic, Phys. Lett. B **571**, 75 (2003); Phys. Lett. B **572**, 171 (2003).

[98] Heavy Flavor Averaging Group, http://www.slac.stanford.edu/xorg/hfag.

[99] H.-n. Li and S. Mishima, Phys. Rev. D **73**, 114014 (2006).

[100] Y.Y. Charng and H.-n. Li, Phys. Rev. D **71**, 014036 (2005).

[101] T.N. Pham, hep-ph/0610063.

[102] M. Beneke and D. Yang, Nucl. Phys. **B736**, 34 (2006).

[103] M. Beneke and S. Jager, hep-ph/0512101.

[104] M. Beneke and S. Jager, Nucl. Phys. **B751**, 160 (2006).

[105] M. Beneke and M. Neubert, Nucl. Phys. **B675**, 333 (2003).

[106] C.H. Chen, Y.Y. Keum, and H.-n. Li, Phys. Rev. D **66**, 054013 (2002).

[107] H.-n. Li and S. Mishima, Phys. Rev. D **71**, 054025 (2005).

[108] Y. Grossman, Int. J. Mod. Phys. A **19**, 907 (2004).

[109] Y.D. Yang, R.M. Wang, and G.R. Lu, Phys. Rev. D **72**, 015009 (2005).

[110] P.K. Das and K.C. Yang, Phys. Rev. D **71**, 094002 (2005).

[111] C.H. Chen and C.Q. Geng, Phys. Rev. D **71**, 115004 (2005).

[112] C.S. Huang, P. Ko, X.H. Wu, and Y.D. Yang, Phys. Rev. D **73**, 034026 (2006).

[113] A.L. Kagan, Phys. Lett. B **601**, 151 (2004); hep-ph/0407076.

[114] M. Beneke, J. Rohrer, and D. Yang, Nucl. Phys. **B774**, 64 (2007).

[115] C.W. Bauer, D. Pirjol, I.Z. Rothstein, and I.W. Stewart, Phys. Rev. D **70**, 054015 (2004).

[116] P. Colangelo, F. De Fazio, and T.N. Pham, Phys. Lett. B **597**, 291 (2004).

[117] M. Ladisa, V. Laporta, G. Nardulli, and P. Santorelli, Phys. Rev. D **70**, 114025 (2004).

[118] H.Y. Cheng, C.K. Chua, and A. Soni, Phys. Rev. D **71**, 014030 (2005).

[119] W.S. Hou and M. Nagashima, hep-ph/0408007.

[120] M. Beneke, J. Rohrer, and D. Yang, Phys. Rev. Lett. **96**, 141801 (2006).

[121] H.-n. Li, Phys. Lett. B **622**, 63 (2005).

[122] A. Datta et al., Phys. Rev. D **76**, 034015 (2007).

[123] A. Ali et al., Phys. Rev. D **76**, 074018 (2007); Y. Li, C.D. Lu, Z.J. Xiao, and X.Q. Yu, Phys. Rev. D **70**, 034009 (2004).

[124] H.-n. Li, S. Mishima, and A.I. Sanda, Phys. Rev. D **72**, 114005 (2005).

[125] A.J. Buras, R. Fleischer, S. Recksiegel, and F. Schwab, Eur. Phys. J. C **45**, 701 (2006); R. Fleischer, S. Recksiegel, and F. Schwab, Eur. Phys. J. C **51**, 55 (2007).

[126] S. Baek and D. London, Phys. Lett. B **653**, 249 (2007).

[127] M. Gronau, arXiv:0706.2156 [hep-ph].

[128] A.V. Manohar and I.W. Stewart, Phys. Rev. D **76**, 074002 (2007).